In-Situ Synchrotron X-Ray Diffraction of Ultrasonic Microstructural Refinement During Solidification in a Commercial Al–Si–Mg Alloy

KATHERINE E. RADER, ANDREW CHUANG, MARK BOWDEN,
ALAN SCHEMER-KOHRN, JONOVA THOMAS, DILEEP SINGH,
and AASHISH ROHATGI

This study reports the first use of *in-situ* synchrotron X-ray diffraction (SXRD) to study the effects of ultrasonic melt processing (USMP) on phase and grain size evolution during solidification in a commercial Al–Si–Mg casting alloy. USMP is a technique that, when applied to aluminum as it solidifies, can be used to refine the local microstructure of large-scale castings. Analysis of the *in-situ* SXRD data to estimate the average grain size of primary α-Al grains during USMP demonstrates that USMP slows the growth rate of α-Al grains and reduces grain size by 36 pct. There is also evidence that USMP causes the primary α-Al grains to move relative to the X-ray beam; such motion increases the probability of primary α-Al grains colliding and fragmenting. This movement becomes constrained at the onset of the Al–Si binary eutectic, suggesting that USMP ceases to effectively refine the microstructure once the Al–Si binary eutectic begins to form. Complementary laboratory-scale X-ray diffraction (XRD) data were used to correlate the lattice parameters of the α-Al and Si (D-A4) phases with temperature to estimate cooling rate during solidification. Thus, this study can guide the design of novel castings with spatially distributed fine-grained regions produced using local ultrasonic processing.

https://doi.org/10.1007/s11661-025-07939-6

I. INTRODUCTION

ALUMINUM (Al) castings currently account for approximately 60 to 70 pct of the Al used in vehicles and have generated renewed interest with the advent of ultra-large castings in electric vehicles.[1] While the benefits of ultra-large castings include consolidation of parts, thereby reducing production times and costs, cast alloys typically have poorer mechanical properties than their wrought counterparts and can be susceptible to casting defects such as porosity and hot tearing. One approach to improve the as-cast mechanical properties is by refining the microstructure to produce small, equiaxed grains compared to the large, dendritic microstructures that typically form during conventional casting. An additional benefit of these equiaxed microstructures is that they can tolerate more strain than dendritic microstructures with columnar growth, thus reducing their susceptibility to hot tears.[2] Various methods for refining the as-cast microstructures include the use of high thermal conductivity molds, chills, chemical grain refiners, and ultrasonic melt processing (USMP).[3–5] The benefits of USMP compared to these other methods are that (1) USMP does not require any chemical additions or modifications to the alloy chemistry, and (2) USMP can achieve smaller grain sizes than those that can be produced using the other methods.[3–5]

Recently, the authors used USMP to refine the local microstructure of A356 aluminum castings by applying sonication to alloy as it solidified within a permanent mold, see Figure 1.[6] This approach is different from most other applications of USMP, where ultrasound is applied to the melt before or during pouring. Applying ultrasound to the alloy during solidification allows for the active application of the ultrasound field to targeted locations within a larger casting during the casting process itself and is intended to be applied to shaped castings (*e.g.,* automotive, aerospace, *etc.* applications).

KATHERINE E. RADER, MARK BOWDEN, ALAN SCHEMER-KOHRN, and AASHISH ROHATGI are with the Pacific Northwest National Laboratory, 902 Battelle Blvd, Richland, WA 99354. Contact e-mails: Katherine.Rader@pnnl.gov; Aashish.Rohatgi@pnnl.gov ANDREW CHUANG, JONOVA THOMAS, and DILEEP SINGH are with the Argonne National Laboratory, 9700 S Cass Ave, Lemont, IL 60439.

Manuscript submitted May 6, 2025; accepted August 1, 2025.

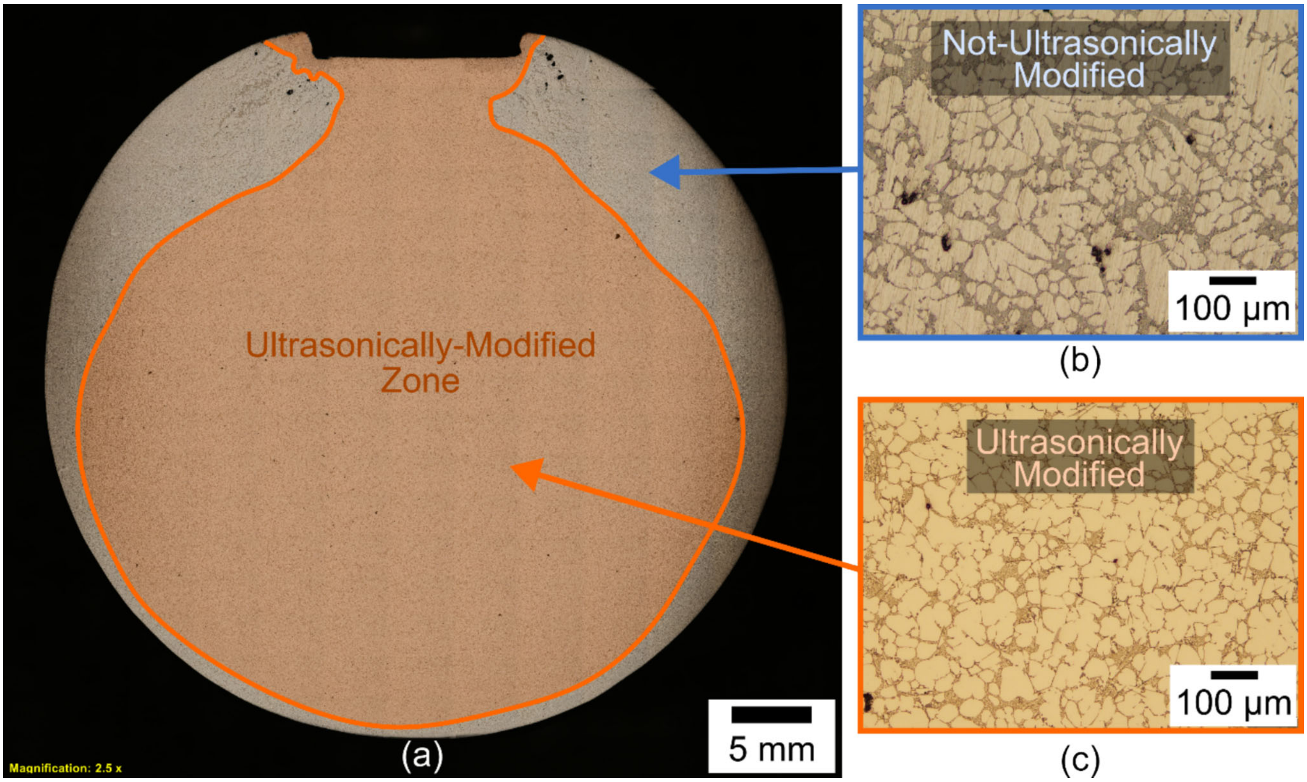

Fig. 1—(*a*) The stitched optical micrograph demonstrates the application of USMP to produce an area of local refinement in a cylindrical, 356 aluminum casting 45 mm in diameter. Optical micrographs show examples of (*b*) the unmodified morphology outside of the ultrasonically modified zone and (*c*) the globular morphology within the ultrasonically modified zone.

This means that in the final casting/component, the region of ultrasonic grain refinement will be localized to a specific location that has a different microstructure than the rest of the casting. For example, local ultrasonic processing could be incorporated into an existing permanent mold casting process to provide enhanced strength and ductility at a local region within the part where fatigue is a concern.

The mechanisms by which USMP produces non-dendritic, refined microstructures can be classified into two categories: (1) those that relate to enhanced nucleation and (2) those that relate to the fragmentation/modification of dendrites. When USMP is applied at temperatures above the liquidus, ultrasonication increases the wettability of small impurities in the melt, increasing the number of potential heterogeneous nucleation sites.[7–10] This enhanced nucleation increases the number of primary Al grains in a given volume of material, thereby decreasing average as-cast grain size.[7–11] When USMP is applied at temperatures below the liquidus (*i.e.*, when the material is semi-solid), the dendrites are fragmented into smaller-sized grain units as a result of mechanical deformation from the implosion of ultrasound cavitation bubbles, the movement of clouds of ultrasound cavitation bubbles, and/or acoustic flow.[12–15]

Several time-resolved, *in-situ* studies have been conducted to study the mechanisms by which USMP refines the microstructures of cast Al alloys. Some of these earliest studies used *in-situ* synchrotron X-ray radiography to observe ultrasonic cavitation in fully molten Al–Cu alloys.[15–17] More recently, *in-situ* synchrotron X-ray radiography and tomography were used to observe USMP applied to semi-solid Al–Cu alloys.[14,18] However, these radiography studies used model Al–Cu alloys that contained high Cu (10 to 35 wt pct) rather than Al–Si–Mg alloys that are routinely used in automotive applications. Model high-Cu alloys were used in these radiography studies to simplify analysis because there is greater phase contrast between Al & Cu than there is between Al & Si, on account of the greater atomic number difference between Al & Cu than Al & Si. In another study, Wang *et al.* used high-speed optical imaging to study the fragmentation of primary crystals *in situ* by using water as a surrogate for liquid Al.[19]

Regarding the use of *in-situ* synchrotron X-ray diffraction (SXRD), various studies have been conducted to characterize the evolution of microstructures formed during the solidification of materials such as Inconel, stainless steel, multi-principal component alloys,[20–24] and Al–Si alloy refined with Ti-based grain refiners.[25] The use of SXRD offers crystalline information, such as phase identification, which X-ray imaging techniques (such as radiography) cannot offer. However, ultrasonication was not employed in these SXRD studies. Most recently, *in-situ* SXRD was used to study USMP applied to a wrought 4xxx Al alloy that was melted *via* laser and cooled at very fast rates of up to

1000 °C/s.[26] However, phase and grain size evolution during solidification were not addressed in that work.[26]

This study seeks to expand upon these previous studies by using time resolved, *in-situ* SXRD to study the microstructural evolution associated with ultrasonically induced grain refinement in a commercial A356 Al casting alloy. Since phase contrast is not a concern for XRD techniques, SXRD is well suited to study Al–Si–Mg alloys as the Al and Si diffraction patterns/peaks can be easily distinguished from one another. Specimens of molten alloy solidified at cooling rates of ~ 1 °C/s that are relevant to permanent mold casting techniques.[27] *In-situ* SXRD allowed for the identification of individual phases (*e.g.,* primary α-Al and eutectic Si) during solidification, enabling us to determine how ultrasound affected their evolution and grain size. Post-mortem electron backscatter diffraction (EBSD) was used to measure the grain size of the ultrasonicated specimen for comparison against that estimated from *in-situ* data. Complementary laboratory-scale XRD experiments were conducted to measure the lattice parameters of the Al and Si phases at elevated temperatures. The resulting temperature-lattice parameter calibrations were used to estimate cooling rates during the *in-situ* SXRD experiments. This work is unique in two ways. First, this work studies a commercial-grade cast A356 (Al–Si–Mg) alloy that is routinely used in commercial automotive applications. This alloy may behave differently or exhibit a different microstructural evolution than previously studied model Al–Cu alloys,[14–18] especially in the semi-solid state, as it has different binary eutectic temperatures, form different inter-dendritic structures, and may contain additional ternary phases. Second, this study uses 2D diffraction patterns to quantify grain size evolution *in-situ*, which was not reported in prior SXRD studies.[20–26] Such quantifications can provide more insights about the mechanisms governing ultrasonically induced microstructural refinement of primary Al grains in cast Al alloys and the temperature regime for effective refinement during local USMP.

II. EXPERIMENTAL

A. *Material*

The material studied was a commercial-grade A356 aluminum alloy (Al–Si–Mg) received from Belmont Metals Inc. The composition of the alloy, according to the manufacturer, is listed in Table I.

Previous work used thermodynamic simulations to predict the phases expected in a similar A356 alloy that solidified at a cooling rate of 1.4 °C/s using the Al material database (CompuTherm) and microstructural model in ProCAST.[6] The following predictions are according to a back diffusion model, though a Scheil model was also considered: the calculated liquidus of the alloy is 616 °C, the calculated Al–Si binary eutectic temperature is 573 °C, and the calculated solidus is 554 °C.[6] The most prevalent phases that were predicted to form, along with their respective crystal system and space group, are listed in Table II.

Table I. Composition of the Alloy in Wt Pct

Si	Mg	Cu	Zn	Cr	Mn	Ti	Fe	Al
7.05	0.41	0.01	0.01	0.01	0.01	0.14	0.09	bal.

B. *Laboratory-Scale X-Ray Diffraction*

Laboratory-scale X-ray diffraction (XRD) experiments were conducted using a Panalytical MPD equipped with an Anton Paar HTK-1200 hot stage at Pacific Northwest National Laboratory to measure the lattice parameter of the phases in the A356 alloy as a function of temperature. Specimens of the A356 alloy and Al_2O_3 were cut and polished to the same size and height. The specimens were placed next to one another on the hot stage, each occupying approximately the same irradiated area, and heated simultaneously. A 10 mm × 10 mm area was irradiated from a Cu anode ($\lambda\ K\alpha\ =\ 1.5418$ Å) passing through variable divergence and anti-scatter slits. Diffraction data were collected from both materials at nominal temperatures of 30, 300, 400, 500, 550, and 600 °C. While a thermocouple was used to monitor and help regulate the temperature of the hot stage, it was not in contact with the specimens or the hot stage itself. Therefore, the actual temperature of the A356 specimen at each set temperature was calibrated using the lattice parameter, c, of the Al_2O_3 specimen and thermal expansion data from Reference 29.

C. *In-Situ Synchrotron X-Ray Diffraction*

In-situ synchrotron X-ray diffraction (SXRD) experiments were conducted at beamline 1-ID-E at the Advanced Photon Source at Argonne National Laboratory. A detailed description of the experimental setup and procedure is provided in Appendix 1.1. In the coordinate system of the experiment, the X-ray beam traveled along the + Z axis and the + Y axis pointed upward (see Figure 2). For the beamline experiments, specimens of A356 alloy (~ 7 g) were melted in an hourglass-shaped fused-quartz crucible using induction heating. The X-ray beam intersected the specimen approximately 2 mm above its base, where the specimen thickness was approximately 4 mm. Ultrasonic melt processing (USMP) was applied *via* a Sonics VCX 750 ultrasonic processor equipped with a tapered, 2-mm-dia. Ti–6Al–4V probe. A Type-K thermocouple was

Table II. Predicted Phases at 545 °C, According to Ref. 6, and Their Symmetry Elements According to Ref. 28

Phase	Predicted Fraction (Wt Pct)	Crystal System	Space Group
α-Al	94.2	cubic	Fm-3m
Si	5.2	cubic	A4
β-(Al_5FeSi)	0.3	monoclinic	
π-($Al_8FeMg_3Si_6$)	0.1	hexagonal	P62m

attached to the tip of the ultrasound probe to measure the temperature of the aluminum alloy adjacent to the probe tip. Both the thermocouple and tip of the ultrasound probe were positioned approximately 10 mm directly above the X-ray beam path through the specimen. A Pilatus3X CdTe 2 M detector positioned downstream of the sample and perpendicular to the incident X-ray beam was used to collect diffraction data. The beam energy was set to 67.416 keV (corresponding to the Ta K-edge) and a 100 × 100 μm square beam was employed. Each frame was acquired with an exposure time of 0.1 second, and a time interval of 0.01 second between frames. A CeO_2 foil was used to calibrate the sample-to-detector distance and to determine the beam center on the detector.

For all experiments, the induction system was operated at the same power output to melt the specimens, and the specimens were kept above the liquidus temperature. The start of each experiment (time $t = 0$ s) was defined as the moment the power to the induction coils was turned off, initiating the cooling of the molten alloy. The ultrasound probe was inserted into the melt in all experiments, regardless of whether ultrasound was applied, to ensure consistent cooling conditions across all tests. Based on the readings from the thermocouple inserted into the melt, the average cooling rate between the calculated liquidus and solidus temperatures was approximately 1 °C/s for both experiments, which falls within the range of cooling rates for permanent mold casting processes.[27] Experiments where USMP was not applied are referred to as the "control" in subsequent sections. In experiments where USMP was applied, ultrasonic processing was applied from when the ultrasound probe was submerged in the specimen at approximately $t = 19$ s until approximately $t = 150$ s, when power to the ultrasound system was stopped. The ultrasound probe oscillated longitudinally at a frequency of 20 kHz. The ultrasonic converter operated at power levels up to 750 W to maintain a constant peak-to-peak amplitude of 82.5 μm at the probe tip. This amplitude value was provided by the vendor, based on their calibration measurements conducted in air using laser vibrometry.

The collected 2D diffraction data were integrated and processed using Pydidas, an open-source software developed at Helmholtz-Zentrum Hereon.[30] A detailed description of the algorithm used to process the data is provided in Appendix 1.2. The 2D diffraction patterns were azimuthally integrated over the angle, χ, from 0 to 360 deg. To address the discontinuous diffraction patterns with only a few diffraction spots observed during the early part of solidification (*i.e.*, when there are only a few primary α-Al grains), a dynamic mask was applied when integrating the α-Al diffraction peaks in Pydidas to mask pixels with low intensity. During integration, radial distance was converted into Q-space, which is related to scattering angle, $2\theta_{\mathrm{hkl}}$, and interplanar spacing, d_{hkl}, using Eq. [1],

$$Q_{hkl} = \left(\frac{4\pi}{\lambda}\right)\sin\left(\frac{2\theta_{hkl}}{2}\right) = \frac{2\pi}{d_{hkl}}, \qquad [1]$$

where Q_{hkl} is scattering vector and λ is the wavelength of the X-ray beam (0.183909 Å).[31] After integration and conversion of the 2D diffraction pattern data into 1D Q_{hkl} *vs* intensity lineout, a first-degree polynomial was used to fit and subtract the background. A pseudo-Voigt function was used to fit diffraction peaks. The peak position was defined as the center of the fitted curve, the peak intensity as the amplitude of the fitted curve after background subtraction, and the peak width as the full width at half maximum (FWHM) of the fitted curve.

1D diffraction patterns integrated from 2D diffraction patterns obtained when the specimens were fully solidified were used to identify the phases present in the material studied. Diffraction peaks were identified by comparing peak locations, determined using Pydidas, to known phases in the ICDD database.[32] As both the α-Al and Si phases are cubic, the lattice parameters of these phases, a, were calculated from their respective indexed diffraction peaks using Eq. [2],

$$a = \sqrt{h^2 + k^2 + l^2}\left(\frac{2\pi}{Q_{hkl}}\right). \qquad [2]$$

D. *Microstructural Characterization*

The ultrasonicated specimen from the *in-situ* SXRD experiment was allowed to cool to room temperature, without being remelted, to preserve its microstructure. The orientation of the specimen relative to the X-ray beam was marked on the crucible. The specimen was then sectioned in half along its height so that the cut face (*Y–Z* plane, see Figure 2) was parallel to the direction of the X-ray beam. The specimen was polished to a final finish with colloidal silica in preparation for microscopy. EBSD was performed using an Oxford Instruments Symmetry detector on a JEOL IT-800 scanning electron microscope. The accelerating voltage of the electron beam was 20 kV and the working distance was 20.4 mm. A step size of 0.5 μm was used. A total area of 4.27 mm × 0.35 mm was indexed, stitched together, and analyzed *via* Oxford NanoAnalysis Aztec version 6.1. Grains were defined by a high-angle grain boundary threshold of at least 10 deg. Boundary grains were included when calculating the average size of α-Al grains.

Table III. Lattice Parameter of Al and Si Phases, a_{Al} and a_{Si}, at Various Calibrated Temperatures, as Determined by Laboratory-Scale XRD

Calibrated Temperature (°C)	a_{Al} (Å)	a_{Si} (Å)
33.5	4.0532	5.4340
277	4.0793	5.4379
374	4.0900	5.4391
466	4.1022	5.4415
532	4.1074	5.4422
576	N/A	N/A

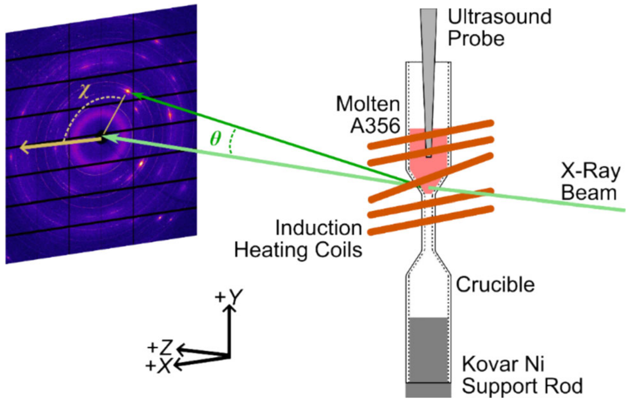

Fig. 2—Schematic drawing of the hourglass-shaped fused-quartz crucibles used for *in-situ* SXRD experiments (image not to scale).

III. RESULTS

A. *Temperature-Lattice Parameter Correlation*

To estimate the temperature of the specimens during the *in-situ* SXRD experiments from the lattice parameters of the Al and Si phases, complementary laboratory-scale X-ray diffraction (XRD) experiments were conducted. The lattice parameters of the Al and Si phases, a_{Al} and a_{Si}, measured at various temperatures using XRD are listed in Table III. Temperature during XRD was calculated from linear expansion along the *c* axis of the α-Al_2O_3 specimen that was heated and exposed to X-rays simultaneously with the A356 specimen. When the temperature of the A356 specimen reached 576 °C, diffraction peaks from both the α-Al and Si phases disappeared and a single, diffuse diffraction peak from an amorphous phase was observed. This disappearance of the α-Al and Si diffraction peaks indicates that at 576 °C the diffracting α-Al and Si grains had melted. Because this temperature is below the liquidus of the alloy (616 °C) but above the temperature of the Al–Si binary eutectic (573 °C[6]), the disappearance of the α-Al and Si diffraction peaks suggests that the eutectic α-Al and Si grains were the primary source of diffraction intensity during XRD. This is despite the relatively large size of the primary α-Al grains, which would not be expected to fully melt until a higher temperature (616 °C). The temperature-lattice spacing data in Table III were fit to the following second-degree polynomials that can be used to estimate a_{Al} and a_{Si} from temperature, *T*, in Kelvin:

$$a_{\mathrm{Al}} = 6.356 \times 10^{-9} T^2 + 1.036 \times 10^{-4} T + 4.021 \qquad [3]$$

$$a_{\mathrm{Si}} = 4.891 \times 10^{-9} T^2 + 1.133 \times 10^{-5} T + 5.430 \qquad [4]$$

B. *Phase Identification*

Thermodynamic calculations from previous work related to this study identified the expected phases, in an A356 alloy of similar composition,[6] to include the α-Al, Si (D-A4), β-Al_5FeSi, and the π-$Al_8FeMg_3Si_6$ phases (see Table II). However, only the α-Al and the Si (D-A4) phases were detected *via in-situ* SXRD in this work. The absence of phases other than α-Al and Si suggests that there were not enough diffracting grains to detect the Fe-containing intermetallic phases. For the control specimen (*i.e.*, produced without USMP), the α-Al and Si (D-A4) phases accounted for all of the identifiable diffraction peaks. For the ultrasonicated specimen, there were additional weak diffraction peaks at $Q = 14.45\ \mathrm{nm}^{-1}$, $15.60\ \mathrm{nm}^{-1}$, and $17.81\ \mathrm{nm}^{-1}$. The diffraction peak at $Q = 17.81\ \mathrm{nm}^{-1}$, which first appears at $t \approx 115$ s, may be Al_2O_3. It is possible that a layer of Al_2O_3 that was thick enough to diffract formed on the outer surface of the ultrasonicated specimen as a result of long exposure time to high temperatures. The other weak diffraction peaks at $Q = 14.45\ \mathrm{nm}^{-1}$ and $Q = 15.60\ \mathrm{nm}^{-1}$ did not correspond to any known phases containing Al, Si, Mg, and/or Fe, including the β-Al_5FeSi, π-$Al_8FeMg_3Si_6$, Al_3Ti, Mg_2Si, β′-Mg_2Si, $SrAl_2Si_2$, Si_2V, and Al_3Zr phases. The intensity of these unindexed diffraction peaks and the diffraction peak at $Q = 17.81\ \mathrm{nm}^{-1}$ were weak relative to the other phases present, which suggests that they may be attributed to some sort of contaminant.

C. *2D Diffraction Pattern Analysis*

Video stills of 2D diffraction patterns from the control and ultrasound experiments are shown in Figure 3. Full videos are provided in the electronic supplemental material in the online version of the article. For the control experiment, large diffraction spots corresponding to the α-Al phase first appeared 27 seconds after the specimen began cooling ($t = 27$ s). This event signified that the material had cooled to at least the liquidus, 616 °C. (Note that the specimen may have reached the liquidus earlier. This is further discussed in Section IV–A.) These diffraction spots were "fixed," meaning that once they appeared they did not change in position (*i.e.*, azimuthal angle, χ, or radial distance, *Q*). For the ultrasound experiment, small diffraction spots corresponding to the α-Al phase also first appeared 27 seconds after the specimen began cooling ($t = 27$ s). Unlike the control experiment, however, the diffraction spots appeared to "move," *i.e.*, they rapidly appeared, disappeared, and then reappeared at different azimuthal angles as the material continued to cool and solidify in the presence of ultrasound.

To demonstrate the apparent motion (*i.e.*, their seemingly random appearance/disappearance) of the diffraction spots during the ultrasound experiment in comparison to the "fixed" diffraction spots during the control experiment, the intensity of the α-Al (200) diffraction plane ($Q \approx 3.1\ \mathrm{\mathring{A}}^{-1}$) is plotted as a function of azimuthal angle, χ, and time in Figure 4. For the control experiment, two diffraction spots appeared at $\chi = -146$ deg and 124 deg at the onset of solidification ($t = 27$ s). As time progressed, these spots remained at the same azimuthal angles, producing vertical lines of continuous intensity in Figure 4(a) (see inset *i*). The

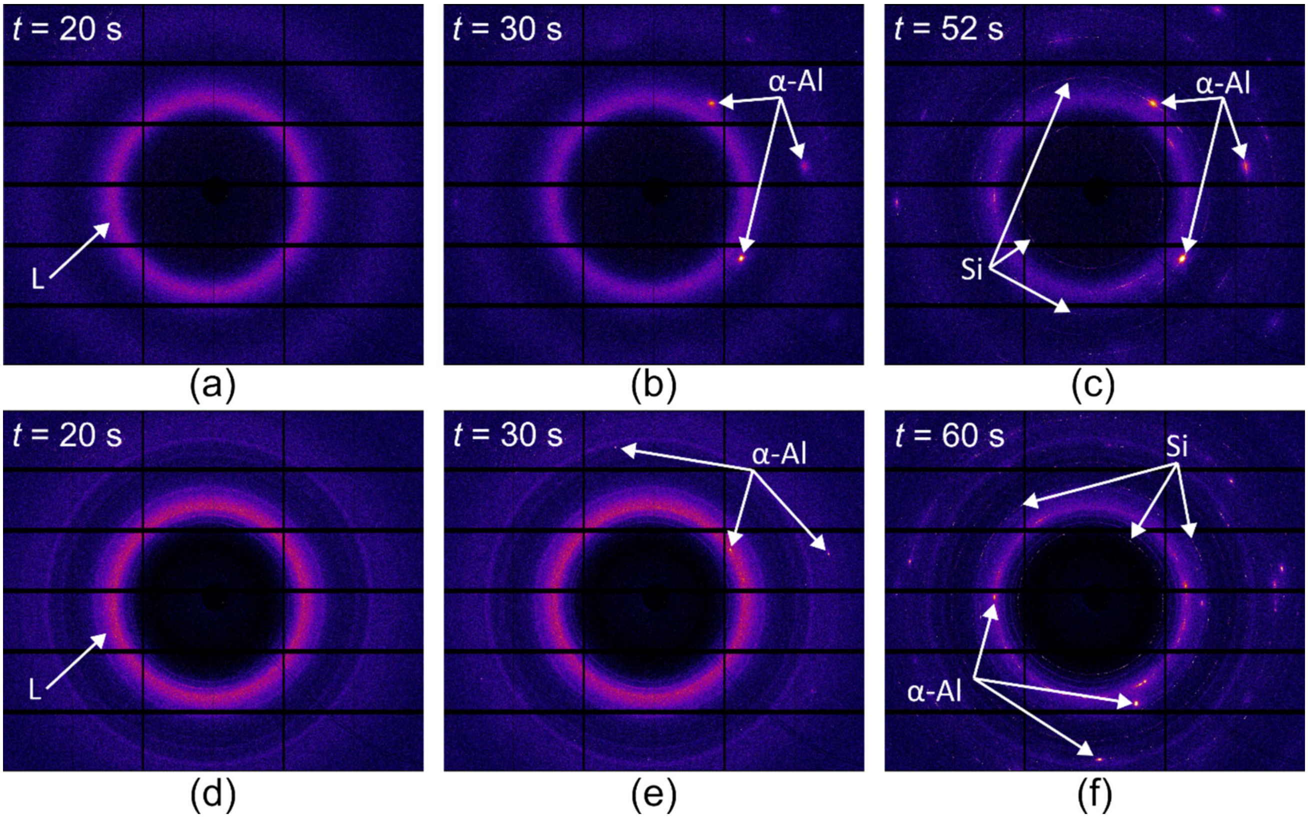

Fig. 3—2D SXRD patterns from (*a*–*c*) the control experiment and (*d*–*f*) the ultrasound experiment. (a, d) correspond to when the specimens were fully molten ($T > 616$ °C), (b, e) correspond to the specimens just after the primary α-Al phase began to form (573 °C $< T <$ 616 °C), and (c, f) correspond to the specimens just after the Al–Si binary eutectic began to form ($T \approx 573$ °C).

persistence of the diffraction spots at the same azimuthal angle in the 2D diffraction patterns (equivalent to vertical lines of continuous intensity in Figure 4) indicates that during the control experiment the diffracting α-Al grains, *i.e.*, crystallites, were stationary relative to the X-ray beam. By comparison, many features in Figure 4(b) suggest that the α-Al grains were physically moving during the ultrasound experiment. During the early stages of solidification in the ultrasound experiment ($t = 27$ s to $t = 33$ s), there were intermittent, individual diffraction spots that did not exist for more than a brief moment (see inset *ii*). The temporal intermittency of the diffraction spots indicates that the diffracting α-Al grains were rapidly moving within the liquid phase, transitioning in and out of the Bragg diffraction condition and possibly in and out of the interaction volume. As another example, at $t = 34$ s, a diffraction spot appeared at $\chi = 73°$ and smoothly shifted about this azimuthal angle, producing a wavy line (see inset *iii*). This line waviness indicates that the diffracting α-Al grain was rotating about an axis parallel to the X-ray beam (*i.e.*, the Z axis).[21] In another instance, at $t = 47$ s, a diffraction spot appeared at $\chi = 114°$, but its intensity fluctuated with time until it disappeared at $t = 53$ s (see inset *iv*). This fluctuation in intensity indicates that from $t = 47$ s to $t = 53$ s, the diffracting α-Al grain moved about an axis perpendicular to the X-ray beam (*e.g.*, the X or Y axes).[21] The absence of any diffraction intensity after $t = 53$ s indicates that the grain moved out of the Bragg diffraction condition. These data provide evidence that the application of ultrasound caused the solid α-Al phase (*i.e.*, primary α-Al grains) to move relative to the X-ray beam within the liquid phase. As the ultrasonicated specimen cooled and the Al–Si binary eutectic began to form, this motion of the α-Al grains became constrained, presumably due to the physical constraints from the eutectic phase and increased viscosity of the melt. A previous radiography study also observed primary α-Al grains moving in a semi-solid Al–Cu alloy when ultrasound was applied, validating our observations that USMP is capable of moving primary α-Al grains within the molten alloy.[14]

For the control experiment, diffraction spots corresponding to the eutectic Si (D-A4) and α-Al phases appeared 47 seconds after the specimen began cooling ($t = 47$ s). The appearance of the Si phase signified that the material had cooled to at least the Al–Si binary eutectic, 573 °C. For the ultrasound experiment, the α-Al diffraction spots no longer change in azimuthal angle at $t = 55$ s [see Figure 4(b)]. At this same time, diffraction spots corresponding to the eutectic Si (D-A4) phase appeared as well as additional α-Al diffraction spots that corresponded to the eutectic Al phase. The

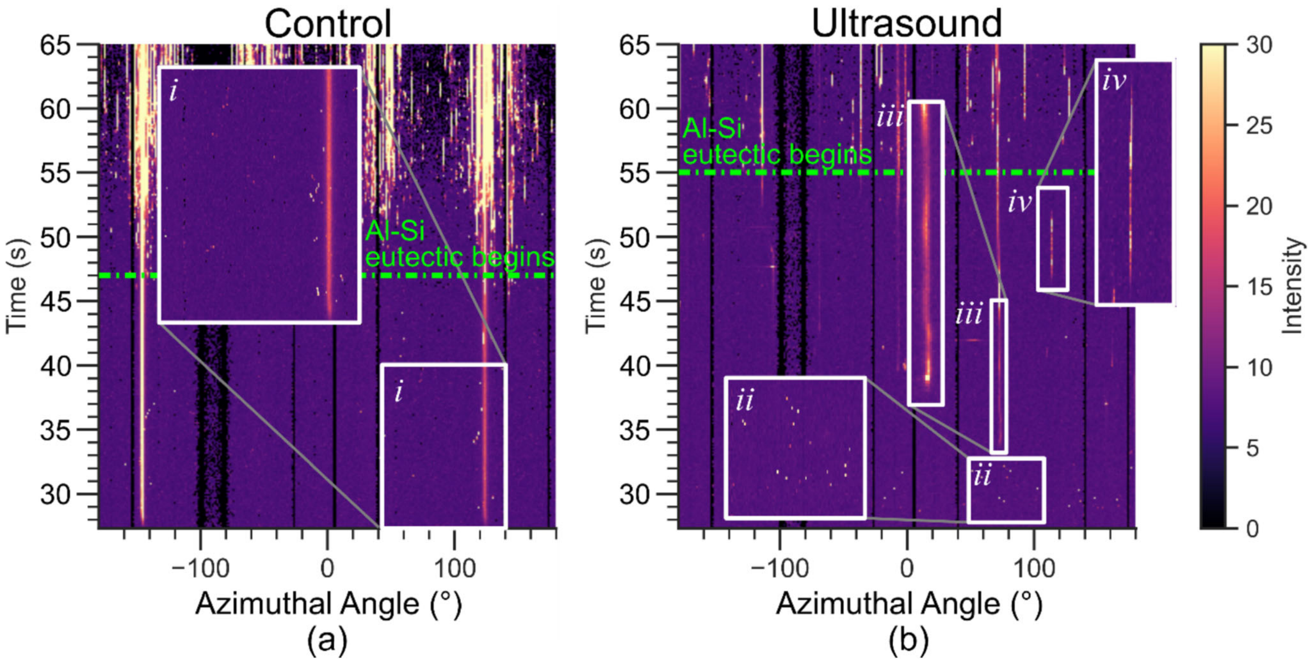

Fig. 4—Intensity of the α-Al (200) diffraction plane ($Q \approx 3.1$ Å^{-1}) plotted as a function of azimuthal angle, χ, and time for (*a*) the control experiment and (*b*) the ultrasound experiment.

fixation of the α-Al diffraction spots indicates that the orientation of the α-Al grains relative to the X-ray beam was no longer changing. Since ultrasound was still being applied to the specimen, the fixation of α-Al spots suggests that a sufficient solid fraction had formed such that ultrasound could no longer move the primary α-Al grains (*i.e.*, they became "stuck" in place).

As can be seen in Figure 3, the diffraction spots corresponding to the primary α-Al phase were smaller and more numerous in the ultrasound experiment compared to the control experiment. In Figure 5, the number of α-Al and Si grains are plotted as a function of time. The number of grains was estimated by taking the total number of distinct diffraction spots around the α-Al (111), (200), (220), and (311) Debye–Scherrer rings and the Si-DA-4 (111), (220), (311), and (422) Debye–Scherrer rings. The number of distinct diffraction spots was counted using radial integration in Pydidas software[30] to plot the intensity as a function of azimuthal angle for each diffraction plane, then counting the number of peaks with an intensity of at least 10 counts above the background. While these counts are not an absolute measure of the number of grains at a given time (as there could be additional grains present that did not satisfy the diffraction condition), they represent an estimate of the lower bound of the number of grains within the interaction volume at a given time. As a note, the data in Figure 5 assume that the number of grains either stays the same or increases with time. This is particularly important for the ultrasound experiment, where the primary α-Al grains were moving relative to the position of the X-ray beam. While it was possible for grains to move in and out of the diffraction condition, it is unlikely that the number of grains decreased during this stage in the experiment (such as from grains melting).

As shown in Figure 5, both the control and ultrasound specimens had a similar number of grains when the α-Al phase began to form. For the control experiment, the number of α-Al grains gradually increased at a rate of 0.6 grains per second until $t = 46$ s. At this time, the number of α-Al grains began to increase exponentially and Si grains began to form (in an exponential manner as well). For the ultrasound experiment, the number of α-Al grains increased in an apparent step-wise manner until $t = 54$ s, after which time the number of α-Al grains began to increase exponentially and Si grains began to form (and increase in number in an exponential manner as well). Between the liquidus and Al–Si binary eutectic reactions, the number of α-Al grains increased, on average, at a rate of 1.8 grains per second during the ultrasound experiment, which is over three times faster than the control experiment (0.6 grains per second). As a reminder, the appearance of Si diffraction data indicates that the Al–Si binary eutectic reaction had begun. For both experiments, the total number of α-Al grains rapidly increased when this reaction began because of the formation of eutectic Al grains, which tend to be smaller and more numerous than the primary α-Al grains, as will be further explained in Section IV–A.

D. *Integrated Diffraction Patterns*

The 2D SXRD patterns for Al and Si (such as those shown in Figure 3) were integrated about the azimuthal angle, χ, (from 0 to 360 deg) to generate 1D SXRD patterns of intensity as a function of radial distance, Q.

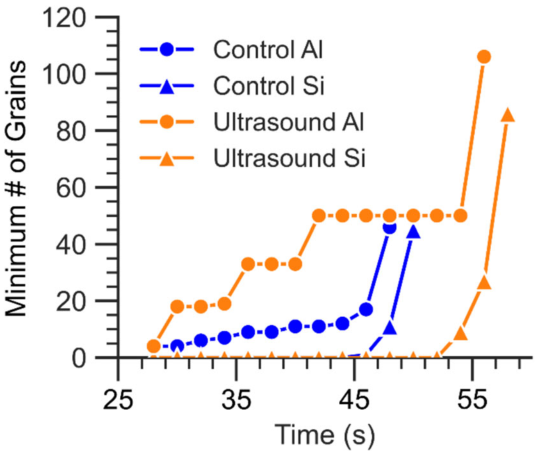

Fig. 5—Lower bound of the number of grains, estimated by counting the total number of discrete diffraction spots, from the time when the α-Al grains began to form until just after the Si eutectic grains began to form (*i.e.*, before the number of diffraction spots became so numerous that they began to overlap and could not be individually distinguished).

Figure 6 summarizes the results for both experiments, with intensity (indicated by color) plotted as a function of Q (horizontal axis) and time elapsed since the specimen began cooling, t (vertical axis). For the control experiment [Figure 6(a)], the Al (200) diffraction peak appeared first. The intensity of this diffraction peak was relatively constant until the Al–Si binary eutectic point was reached at $t \approx 47$ s, at which point it increased. This increased intensity is a result of the formation of eutectic Al grains, which increased the total number of diffracting α-Al grains as shown in Figure 5.

By comparison, the intensity of the Al and Si diffraction peaks in the ultrasound experiment [Figure 6(b)] were less consistent. For example, before the Al–Si binary eutectic was reached at $t \approx 60$ s, the Al diffraction peaks rapidly appeared, disappeared, and reappeared as time increased. This behavior of Al peaks produced the discontinuous intensity highlighted in Figure 6(b) inset, where the integrated diffraction intensity about the location of the Al (111) diffraction peak appears intermittently. Once the Al–Si binary eutectic was reached at $t \approx 60$ s, the intensity of the Al diffraction peaks generally increased (as was also observed in the control experiment). Unlike the control experiment, however, the intensity of the Al diffraction peaks in the ultrasound experiment continued to fluctuate, which may have been a result of the ultrasound probe continuing to vibrate the entire specimen once the Al alloy was fully solidified, thus causing the grains to partially move in and out of the X-ray beam and/or changing their orientation with respect to the X-ray beam.

To determine the lattice parameter of the Al and Si phases during the experiments, a pseudo-Voigt function was fit to the integrated diffraction curves [examples are shown in Figures 6(c) and (d)]. The center of each fitted curve was taken as the position of its corresponding diffraction peak. For the control experiment, the Al (200) and the Si (220) diffraction peaks were used to calculate the lattice parameters of their respective phases, while the Al (111) and the Si (220) diffraction peaks were used for the ultrasound experiment. Although additional diffraction peaks were also identified for both phases, it was difficult to get reliable peak data from these other diffraction peaks (because of their low/inconsistent intensity above the background), especially during the early stages of the solidification (irrespective of control or ultrasound experiment). Figures 6(c) and (d) demonstrate that just after the primary α-Al phase began to form ($t = 30$ s), the α-Al diffraction peaks were relatively weak and did not always have strong intensity. The broad diffraction peak corresponding to the amorphous liquid phase was also still present during the early stages of solidification, which could potentially obscure weak α-Al (111) and (200) diffraction peaks. Another challenge for getting reliable peak data was the inconsistent intensity of diffraction peaks above the background during the ultrasound experiment. For example, as can be seen in Figure 6(b), there were long durations of time before the Al–Si binary eutectic when the integrated intensity of the Al (200) diffraction peak was not discernable. Therefore, the diffraction peaks that provided the most reliable peak analysis for their respective experiments were selected. While using only a single diffraction peak is not sufficient to accurately determine the lattice parameter for a given phase (*e.g.,* (200) or (111) for Al), the spotty nature (*i.e.*, non-uniformity) of the 2D X-ray diffraction patterns (due to the relatively large, and therefore fewer, solidifying grains) produced weak diffraction intensities for other diffraction peaks that could not be reliably used for curve-fitting and accurate determination of the lattice parameter. For additional information regarding the selection of diffraction peaks used to calculate lattice parameter, please refer to Appendix 1.2.

In Figure 7, the lattice parameters of Al and Si (a_{Al} and a_{Si}, respectively) during the control and ultrasound experiments are plotted as a function of time since the specimen began cooling, t. For both experiments, it was expected that a_{Al} would monotonically decrease as the specimen cooled from the liquidus to the Al–Si binary eutectic, remain constant as the Al–Si binary eutectic formed, then continue to monotonically decrease as the specimen continued to cool. For the control experiment, a_{Al} started at ~ 4.110 Å, decreased to ~ 4.105 Å at $t \approx 45$ s, then increased back to ~ 4.110 Å at $t \approx 65$ s. The increase in a_{Al} from approximately 45 to 65 seconds suggests that the primary α-Al grains were undercooled when they initially formed, which is typical of dendritic solidification. As the primary α-Al grains grew in size, they may have slightly warmed to match the temperature of the surrounding bulk material. Subsequently, a_{Al} was relatively constant until it began to continually decrease at $t \approx 100$ s, which likely indicates that the Al–Si binary eutectic finished forming and the temperature of the specimen began to once again decrease. There is a local minimum in a_{Al} at $t = 132$ s after which a_{Al} begins increasing, which corresponds to reheating the specimen for remelting for the next experiment. For

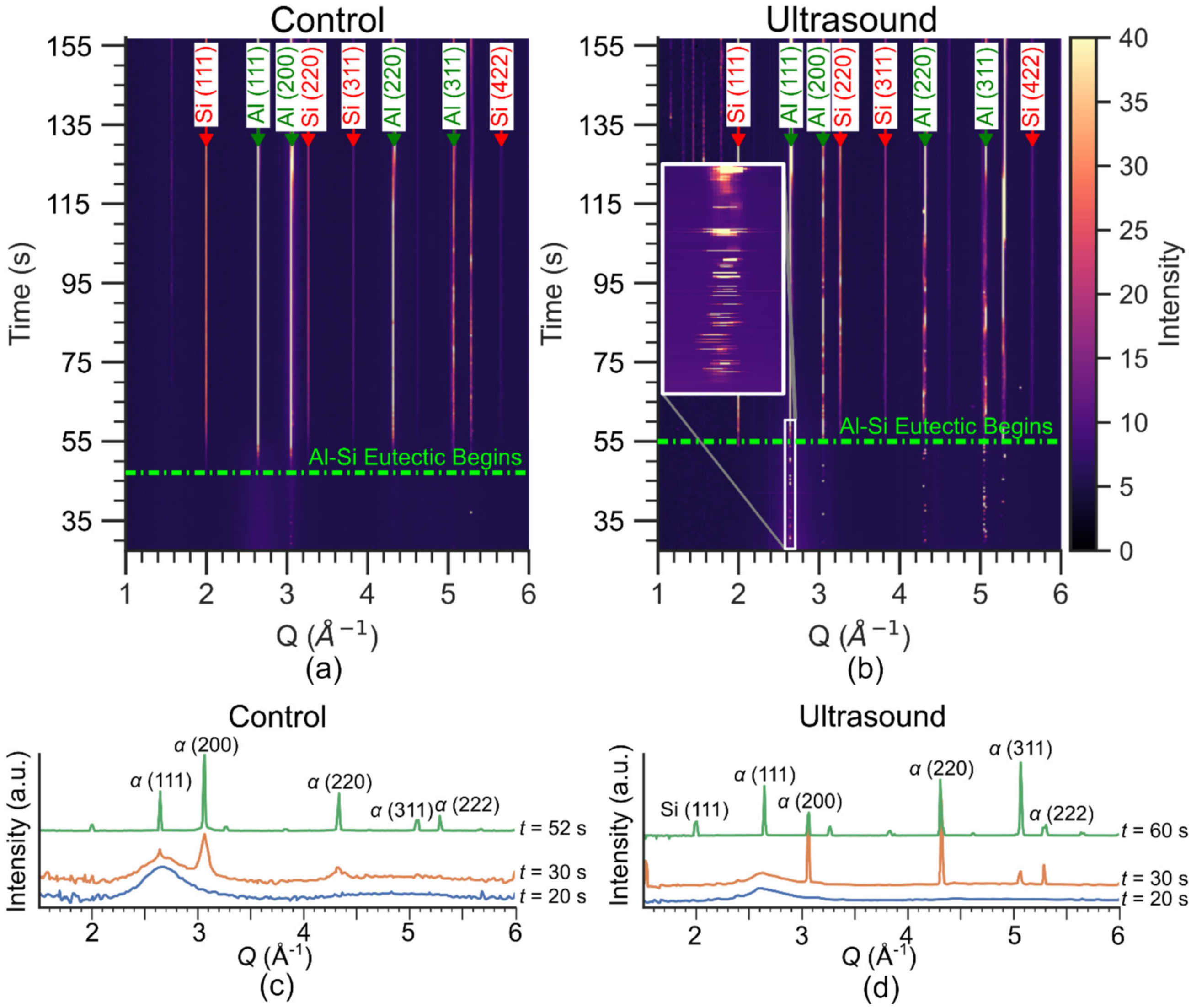

Fig. 6—Integrated synchrotron X-ray diffraction intensity (indicated by color) is plotted as a function of Q-space (horizontal axis), and time elapsed since the start of the experiment, *t* (vertical axis), for the (*a*) control experiment and (*b*) the ultrasound experiment to track the evolution of diffraction peaks. Below these heat maps, integrated diffraction intensity is plotted as a function of Q at select times for (*c*) the control experiment and (*d*) the ultrasound experiment. The data in (c) and (d) were integrated from the same 2D diffraction patterns shown in Fig. 3. For each experiment, diffraction data are presented from $t = 20$ s, when the specimens were fully molten; $t = 30$ s, which was just after the primary α-Al grains began to form; and at $t = 52$ or 60 seconds, which was just after the Al–Si binary eutectic began to form in each respective experiment (Color figure online).

the ultrasound experiment, a_{Al} started, on average, at ~ 4.120 Å, which is 2 pct larger than in the control experiment. This slightly larger lattice parameter could be because the primary α-Al grains were less undercooled than the control experiment or could be partially due to tensile elastic strain on the primary α-Al grains from ultrasound. Unlike the control experiment, where the lattice parameter of Al was relatively constant from 65 to 100 seconds, a_{Al} continually decreased after $t = 65$ s during the ultrasound experiment. This will be further discussed in Section IV–A. For both experiments, the variation in a_{Al} (represented as the error bars in Figure 7) decreases at the onset of the Al–Si binary eutectic. This is likely because the number of α-Al grains increased with the formation of eutectic α-Al grains, thus increasing the intensity of the α-Al diffraction peaks and reducing errors associated with peak fitting.

For both experiments, it was expected that once the Si phase appeared during the Al–Si binary eutectic reaction, a_{Si} would remain constant until the Al–Si binary eutectic was fully formed, after which it would decrease as the specimen cooled below the eutectic. For the control experiment, a pseudo-Voigt curve could not be fit to the Si (220) diffraction peak until $t \approx 52$ s, even though the first Si diffraction data were detected at $t = 47$ s. At $t \approx 52$ s, a_{Si} began at ~ 5.448 Å and gradually decreased until it reached approximately 5.444 Å at $t = 132$ s. As was observed with a_{Al} for the control experiment, there is a local minimum in a_{Si} at $t = 132$ s which corresponds to reheating the sample

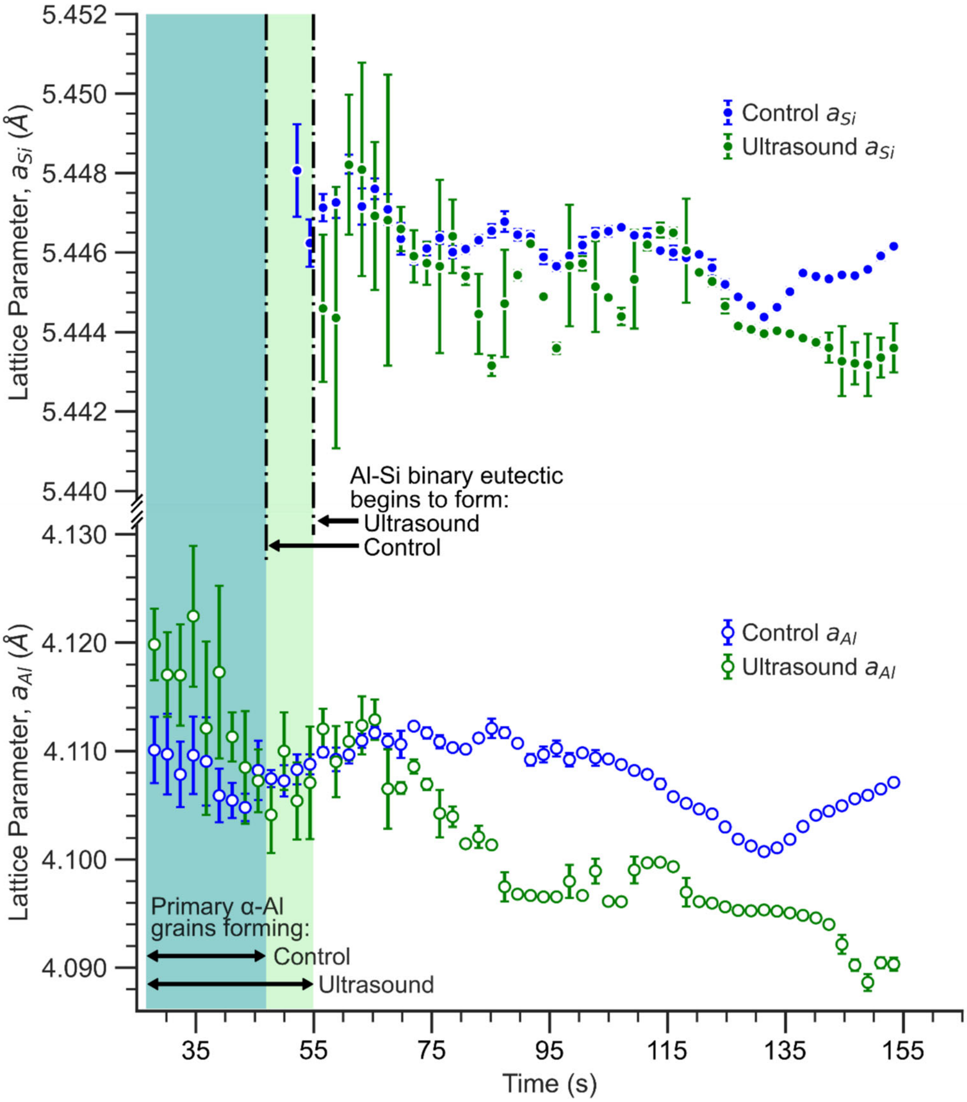

Fig. 7—The lattice parameters of Al and Si (a_{Al} and a_{Si}, respectively) are plotted as a function of time for the control experiment (blue symbols) and ultrasound experiment (green symbols). a_{Al} was measured from the Al (200) diffraction peak for the control experiment and from the Al (111) diffraction peak for the ultrasound experiment. a_{Si} was measured from the Si (220) diffraction peak for both experiments. Note that the scale of the vertical axis is different for a_{Al} and a_{Si}. Individual data points represent the mean over a 2.2 seconds time interval and error bars represent ± SD from the mean (n = 20). Vertical dot-dash lines indicate the time during each experiment when the Al–Si binary eutectic reaction began (Color figure online).

for remelting for the next experiment. For the ultrasound experiment, a_{Si}, began at ~ 5.444 Å, which is 0.07 pct less than the control experiment. From here, a_{Si} increased to ~ 5.448 Å at $t \approx 60$ s, then continually decreased. While the variation in a_{Si} (represented by the error bars in Figure 7) was relatively small for the control experiment beginning from ~ 10 seconds after the Al–Si binary eutectic began to form, the variation in a_{Si} during the ultrasound experiment was quite large and inconsistent. This measurement uncertainty in a_{Si} during the ultrasound experiment will be further discussed in Section IV–A. Within their respective experiments, a_{Al} and a_{Si} followed similar trends once the Al–Si binary eutectic began to form. Unlike the control experiment, there is no simultaneous local minimum in a_{Al} and a_{Si} for the ultrasound experiment. This is because the ultrasound specimen was allowed to continually cool until it fully solidified (*i.e.*, the specimen was not remelted).

E. *Temperature Estimation*

During the *in-situ* SXRD experiments, the temperature at the tip of the ultrasound probe (*i.e.*, 10 mm above the X-ray beam) was measured using a Type-K thermocouple. Thermocouple temperature data from the control experiment are plotted as a function of time from when the specimen began to cool, t, in Figure 8. According to these data, the specimen reached the liquidus temperature, 616 °C, at t = 21 s. The specimen

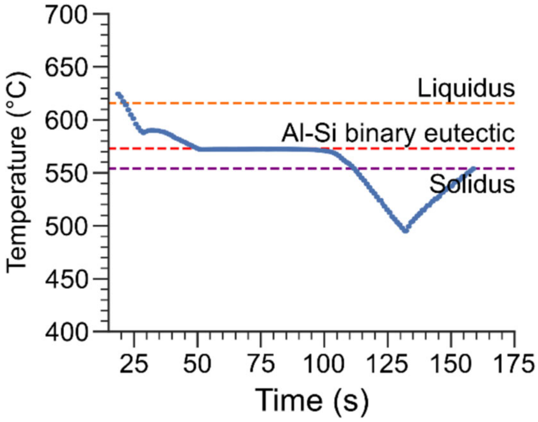

Fig. 8—Temperature during the control experiment, measured from a thermocouple inserted into the melt and positioned approximately 10 mm above the X-ray beam.

then cooled to the Al–Si binary eutectic temperature, 573 °C, at $t = 49$ s. The specimen remained at this temperature as the Al–Si binary eutectic formed until $t = 100$ s, at which point it began to cool again. This plateau and subsequent decrease in temperature suggests that the Al–Si binary eutectic reaction lasted from $t = 49$ s to $t = 100$ s. Temperature continued to decrease until $t = 132$ s, at which point power was resupplied to the induction coils and the specimen began to heat again. According to these thermocouple data, the average cooling rate during solidification (at a position 10 mm above the X-ray beam) for the control experiment was 0.7 °C/s. Temperature data from the ultrasound experiment were not recorded due to technical difficulties. However, recorded observations from the experimental logbook estimate that the ultrasound specimen cooled at an average rate of approximately 0.9 °C/s during solidification. Both of these cooling rates are within the range of cooling rates typical of permanent mold casting processes.[27]

Using the temperature-lattice parameter calibration data in Table III from the laboratory-scale XRD experiments, diffraction data from the *in-situ* SXRD experiments were used to indirectly estimate *in-situ* temperature where the X-ray beam passed through the specimen, T, from the lattice parameters of α-Al and Si (T_{Al} and T_{Si}, respectively). These estimated temperature data are plotted in Figure 9 for both the control experiment and the ultrasound experiment. As a reminder, the induction coils were turned back on during the control experiment to remelt the specimen for the next run, producing a local minimum in the control experiment temperature at $t = 132$ s. For the ultrasound experiment, the specimen was not remelted and was allowed to cool over the entire duration of the experiment. As a note, temperature estimated from the primary α-Al grains (*i.e.*, temperature estimated from a_{Al} before the Al–Si binary eutectic) can have a large error. This is because the thickness of the specimens (> 4 mm) and few number of primary α-Al grains before the Al–Si binary eutectic resulted in a sample-detector distance uncertainty of ± 2 mm, which correlated with a temperature measurement uncertainty of ± 93 °C. The eutectic α-Al and Si grains, however, were presumed to be evenly distributed through the thickness of the specimen, so that the average position of the diffracting α-Al and Si grains could be assumed to be the center of the specimen.

For both experiments, it was expected that T would decrease until the Al–Si binary eutectic reaction began. T would then be approximately constant until the Al–Si binary eutectic finished forming, at which point it would begin to decrease (as was observed in Figure 8). Given the estimated cooling rates of each experiment (according to thermocouple data), T was expected to reach the solidus, 554 °C, at $t \approx 115$ s for the control experiment and $t \approx 95$ s for the ultrasound experiment. However, since the X-ray beam passed through a narrower portion of the specimens than where the thermocouples were located, it was likely that the cooling rates estimated from the lattice parameters of α-Al and Si would be faster. According to the estimated temperature data in Figure 9, it took approximately 83 and 43 seconds for the control and ultrasound specimens, respectively, to solidify. These solidification times correlate with average cooling rates during solidification of 0.7 °C/s for the control experiment and 1.4 °C/s for the ultrasound experiment. Both of these cooling rates are similar to cooling rates typical of permanent mold casting processes.[27] It is interesting that the application of ultrasound appears to increase cooling rate, especially considering that the application of ultrasound also delayed the onset of the Al–Si binary eutectic reaction. Possible explanations for this increased cooling rate will be further discussed in Section IV–A.

F. *Microstructure*

The microstructure of the ultrasonicated specimen from the *in-situ* SXRD experiment was preserved so that it could be characterized *via* post-mortem microscopy. The inverse pole-figure (IPF) map (produced *via* EBSD) shown in Figure 10 includes the cross-sectional area of the ultrasonicated specimen where the synchrotron X-ray beam passed through the specimen during the *in-situ* SXRD experiment. Optical micrograph subsets in Figure 10 highlight the different phases present in the specimen. In the optical micrographs, the α-Al phase appears yellow, the Si phase appears dark brown, and pores appear black. The mean equivalent circle diameter of the primary α-Al grains within the IPF map is 83 ± 76 μm and the area-weighted mean diameter is 209 μm. The optical micrograph subsets in Figure 10 suggest that the X-ray beam may have passed through a mixture of smaller ultrasonically modified and larger unmodified α-Al grains The morphology of the α-Al grain in the upper right corner of subset *i* appears to have a dendritic morphology while the α-Al grains in subset *ii* all appear to have a globular morphology.

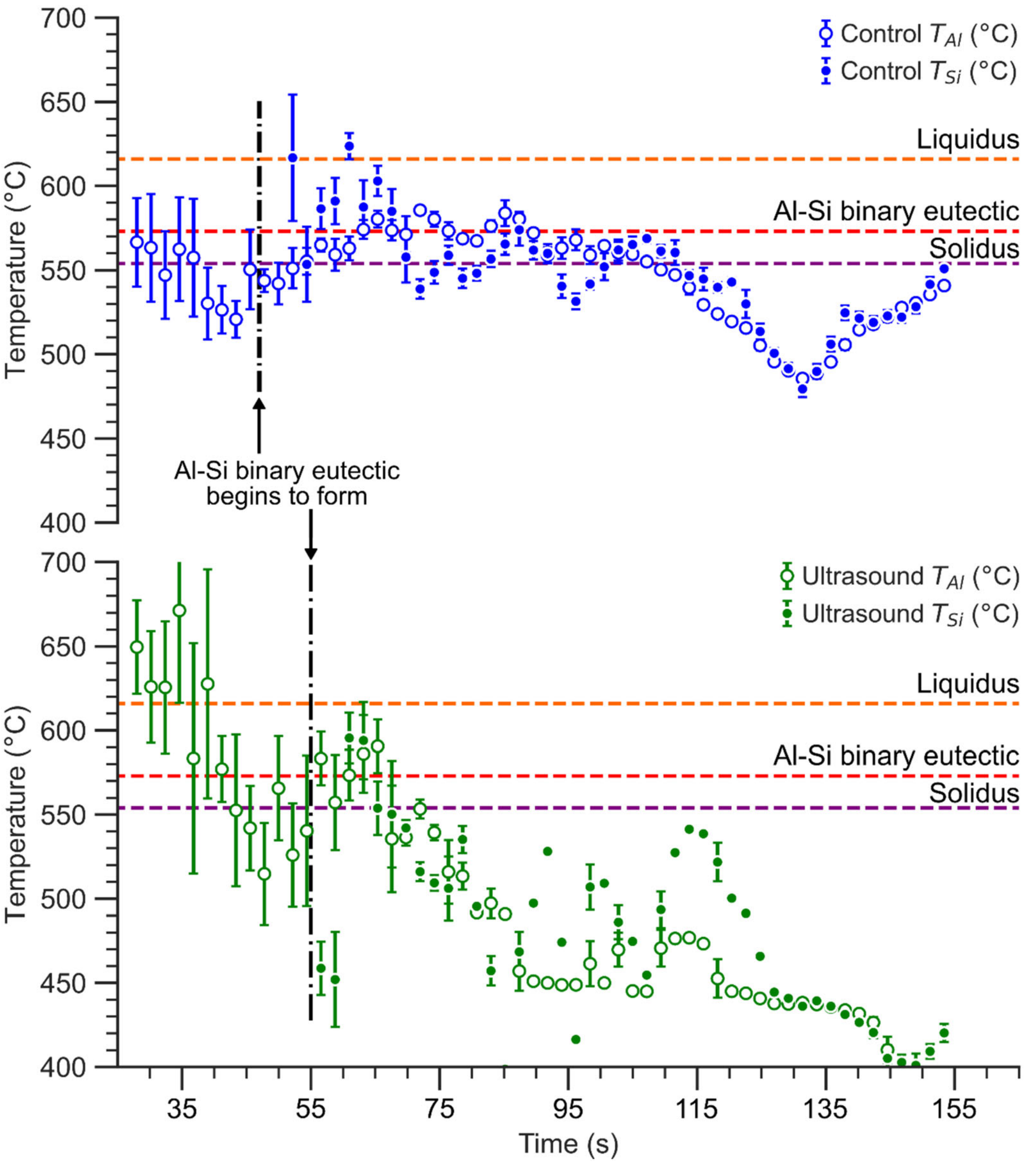

Fig. 9—Temperature, calculated from the lattice parameters of α-Al (represented by empty circles) and Si (represented by filled circles), for the control experiment (blue symbols) and ultrasound experiment (green symbols). Individual data points represent the mean over a 2.2-s time interval and error bars represent ± SD from the mean ($n = 20$). Vertical dot-dash lines indicate the time during each experiment when the Al–Si binary eutectic reaction began (Color figure online).

IV. DISCUSSION

A. *Evolution of Phases During Solidification*

The evolution of phases during the solidification of A356 aluminum alloy is visually summarized in Figure 11. At the beginning of the experiment, when the temperature of the alloy is above 616 °C, the alloy is fully molten. Once the alloy cools to the calculated liquidus temperature, 616 °C, the primary α-Al phase begins to form. If ultrasonic processing is being applied to the alloy, then the α-Al grains are able to move within the liquid phase until just before the Al–Si binary eutectic begins to form at 573 °C. The primary α-Al grains are larger than eutectic Al grains and typically have a dendritic morphology under conventional casting conditions, as shown in Figure 1(b). If ultrasonic processing is applied during solidification, then the primary α-Al grains will have a globular morphology within the region of ultrasonic refinement, as shown in Figure 1(c). This region of ultrasonic refinement is adjacent to the tip of the ultrasound probe and can extend as far as 40 mm away, as shown in Figure 1(a).[6] Below the Al–Si binary eutectic temperature, other intermetallic phases will form (*e.g.*, β-Al_5FeSi, π-$Al_8FeMg_3Si_6$, *etc.*) until the solidus is reached.[6] Thus, the fully solidified, as-cast microstructure typically consists of primary α-Al grains surrounded by smaller Al eutectic grains, Si eutectic grains, and various

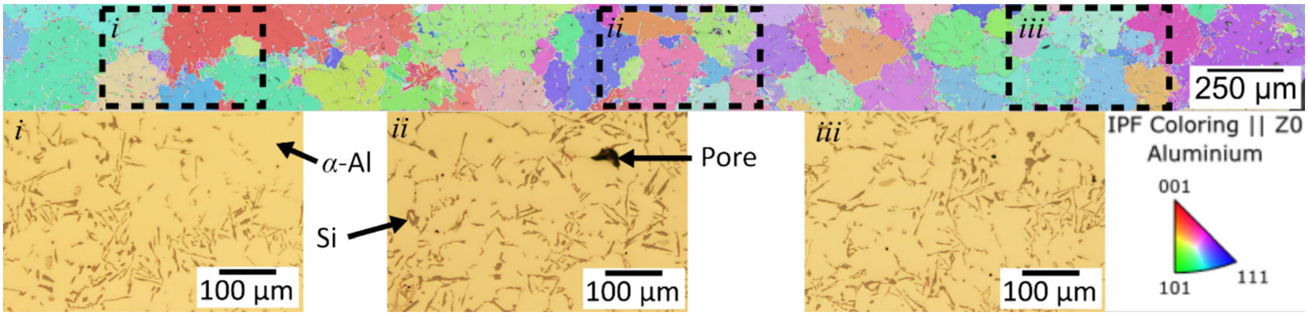

Fig. 10—The stitched EBSD inverse pole-figure map depicts the solidified microstructure of the ultrasonicated specimen from the *in-situ* synchrotron X-ray diffraction experiment. The horizontal axis of the image is parallel to where the X-ray beam passed through the specimen and the vertical axis of the image is parallel to the height of the specimen. Optical micrographs highlight the different phases present in various subsets of the area in the IPF map: α-Al (yellow) and Si (dark brown) (Color figure online).

intermetallic phases. For both the control and ultrasound *in-situ* synchrotron experiments in this study, X-ray diffraction peaks corresponding to the predicted intermetallic phases were not detected. Given the high energy of the synchrotron X-ray beam and the sensitivity of the detector used, it is highly unlikely that the low fraction of these phases (less than 3 wt pct, see Table II) is the reason why these phases could not be detected. Rather, it is more likely that there were not sufficient grains satisfying the Bragg diffraction condition to produce a discernable diffraction intensity above the background.

For both the control and ultrasound *in-situ* experiments, the first diffraction data from a solid phase were detected 27 seconds after the specimens began cooling, suggesting that both specimens cooled at approximately similar rates before the onset of solidification. However, for the control experiment, the thermocouple recorded that the temperature of the specimen reached the liquidus, 616 °C, 6 seconds earlier. The difference in time between these two events suggests that the time at which the first solid phase is detected may not correspond with the onset of solidification. This may be because the first grains to form did not satisfy the Bragg diffraction condition. Another possible explanation may be that diffraction from the solid α-Al grains during the early stages of solidification is obscured by the diffuse diffraction peak of the amorphous liquid phase. When the aluminum alloy is fully liquid, there is a diffuse diffraction peak that extends from $Q = 2.2$ Å^{-1} to 3.3 Å^{-1}, which overlaps with the diffraction of the α-Al (111) ($Q \approx 2.6$ Å^{-1}) and (200) ($Q \approx 3.1$ Å^{-1}) planes [see Figures 6(c) and (d)].

While the α-Al phase began to diffract at the same time in both the control and ultrasound experiments, the Si phase took ~ 8 seconds longer to begin diffracting in the ultrasound experiment. Since the formation of the Si phase corresponds with the onset of the Al–Si binary eutectic reaction, this delay suggests that the ultrasonicated specimen cooled more slowly than the control specimen between the liquidus and Al–Si binary eutectic. However, temperature estimated from the lattice parameters of α-Al and Si (Figure 9) suggest that the ultrasound specimen cooled at a faster rate than the control experiment. Wang *et al.*[26] observed a similar increase in cooling rate when ultrasonic treatment was applied to a weld pool. They attributed this increased cooling rate to enhanced latent heat dissipation by stirring from acoustic streaming. It is therefore likely that the Al–Si binary eutectic may have actually begun to form at a time earlier than $t = 55$ s, but diffraction data were not detected from the eutectic Si phases because of their small volume fraction and movement due to acoustic streaming and agitation from ultrasound. Once the total solid fraction (primary α-Al + eutectic α-Al + eutectic Si) reached a critical level at which acoustic streaming could no longer move the solid grains within the remaining liquid, the movement of the grains ceased. There were then sufficient Si grains within the interaction volume that satisfied the Bragg diffraction condition to produce a continuous, discernable diffraction intensity.

For the control experiment, the temperatures estimated from the lattice parameters of α-Al and Si were in relatively close agreement and, once the Al–Si binary eutectic began for form, followed similar trends as the temperature data measured from the thermocouple. For the ultrasound experiment, however, there was more variation in the temperatures estimated from the lattice parameters (indicated by the error bars in Figure 9) and the estimated temperatures fluctuated more than those of the control experiment as time progressed. This larger variation in temperature, as well as the large variation in a_{Si}, during the ultrasound experiment may be a result of the specimen vibrating. During the ultrasound experiment, USMP was applied to the specimen over the entire duration of solidification. As the aluminum solidified, it fused to the ultrasound probe and the entire specimen began to vibrate along with the ultrasound probe. These vibrations could have caused the specimen, and therefore the grains, to translate up to ~ 80 μm along the Y axis, which in turn could cause the intensity of the diffraction peaks to fluctuate. For context, the height of the X-ray beam was 100 μm. It is also possible that the vibrations may have caused the specimen to shift slightly off-axis, which in turn could affect the sample-detector

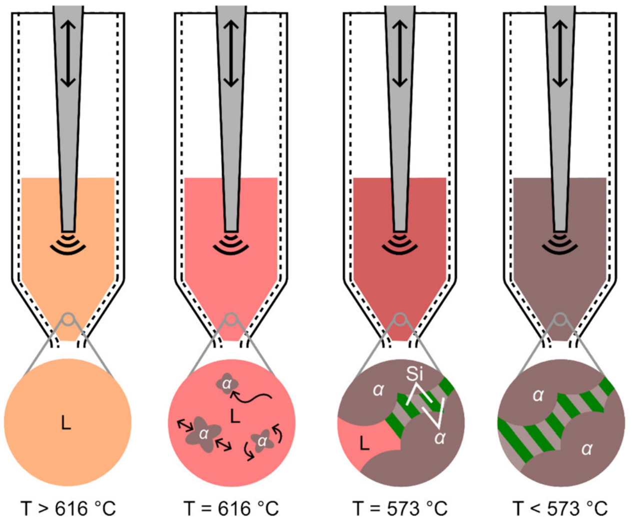

Fig. 11—Schematic representation of the evolution of Al and Si phases as the alloy solidified during USMP. Above 616 °C, only the molten liquid phase (L) is present. At 616 °C, primary α-Al grains begin to form and move within the melt. At 573 °C, the primary α-Al grains are stationary and eutectic Al & Si grains begin to form. Below 573 °C, the Al–Si binary eutectic is fully formed. Schematic drawn is not to scale.

distance and would cause the diffraction peak location to shift, resulting in large variation in calculated lattice parameter and apparent temperature.

B. *Evolution of Primary α-Al Grains*

Assuming that the number of discrete diffraction spots at a given time, N_α, is a lower boundary estimate of the number of α-Al grains inside the interaction volume at a given time (see Figure 5), the average size of the α-Al grains at a given time can be estimated. Because the actual number of α-Al grains at a given time could be greater than N_α, the following estimate for the average α-Al grain size should be taken as an upper bound. For the purpose of comparison between the two experiments, it is assumed that the average temperature of the specimen (including the liquid phase and any solid phases), T_{spec}, was 616 °C when the first α-Al diffraction spots were detected and 573 °C when the first Si diffraction spots were detected. It is also assumed that the specimens cooled at a constant rate between 616 °C and 573 °C. The assumed cooling rates between the liquidus and binary eutectic temperatures are therefore 2.2 °C/s for the control experiment and 1.5 °C/s for the ultrasound experiment. (As a note, the cooling rate during this portion of the solidification regime is expected to be slightly faster than the cooling rate over the entire solidification regime.) Using previous data by Rader *et al.*,[6] which used ProCAST to predict solid fraction at a given temperature, the solid fraction of α-Al at a given time can be calculated from this estimate of temperature, T_{spec}. These data are plotted in Figure 12(a).

The size of the interaction volume, V, is equal to the cross-sectional area of the X-ray beam, 100 × 100 μm, times the thickness of the specimen where the X-ray beam passed through, ~ 4 mm. From this total volume, the total volume of α-Al phase at a given time, V_α, can be calculated using the estimated solid fraction of the α-Al phase, f_S. Assuming that the average volume of each individual α-Al grain, $\overline{V_\alpha}$, is equal to V_α/N_α, then the average diameter of each α-Al grain, $\overline{d_\alpha}$, can be calculated using the following equation:

$$\overline{d_\alpha} = 2\left(\frac{3\overline{V_\alpha}}{4\pi}\right)^{(1/3)} = 2\left(\frac{3Vf_S}{4\pi N_\alpha}\right)^{(1/3)} \qquad [5]$$

The average diameter of the α-Al grains, estimated using Eq. [3], is plotted as a function of time since the specimens began cooling in Figure 12(b). Because these α-Al grains formed before the Al–Si binary eutectic reaction, they can be identified as primary α-Al grains. The initial growth rate, measured from t = 28 s through t = 32 s, of the α-Al grains that formed without ultrasound (initial growth rate = 14 μm/s) is seven times faster than the α-Al that formed with ultrasound (initial growth rate = 2 μm/s). After t = 32 s, the average diameter of the primary α-Al grains was somewhat stable (*i.e.*, $\overline{d_\alpha}$ did not change significantly with increasing time) and the average diameter of the primary α-Al grains formed with ultrasound was consistently smaller than the primary α-Al grains formed without ultrasound. For the control experiment, $\overline{d_\alpha}$ = 139 ± 5 μm from t = 34 s through t = 46 s. For the ultrasound experiment, $\overline{d_\alpha}$ = 90 ± 4 μm from t = 34 s through t = 54 s, which is 36 pct smaller than the α-Al grains formed without ultrasound. Because the average diameter of the primary α-Al grains did not change much after t = 32 s, this suggests that the application of ultrasound to refine the primary α-Al grains is most effective near the onset of solidification. Further application of ultrasound ensured that the primary α-Al grains retained their smaller average grain size as additional grains formed. Therefore, while ultrasound is most effective near the onset of solidification, it may be necessary to apply ultrasound over longer durations of the solidification window in order to achieve the greatest possible degree of grain refinement.

These data demonstrate, *via in-situ* diffraction data, that the application of ultrasonic melt processing reduces the size of primary α-Al grains. Furthermore, the average diameter of the primary α-Al grains just before the Al–Si binary eutectic reaction is estimated to be 94 μm. This estimated diameter is only a few microns different from the average grain diameter of the primary α-Al grains measured post-mortem using EBSD data (83 μm, see Figure 10). This suggests that the size of the primary α-Al grains did not change much once the Al–Si binary eutectic began to form. This observation also

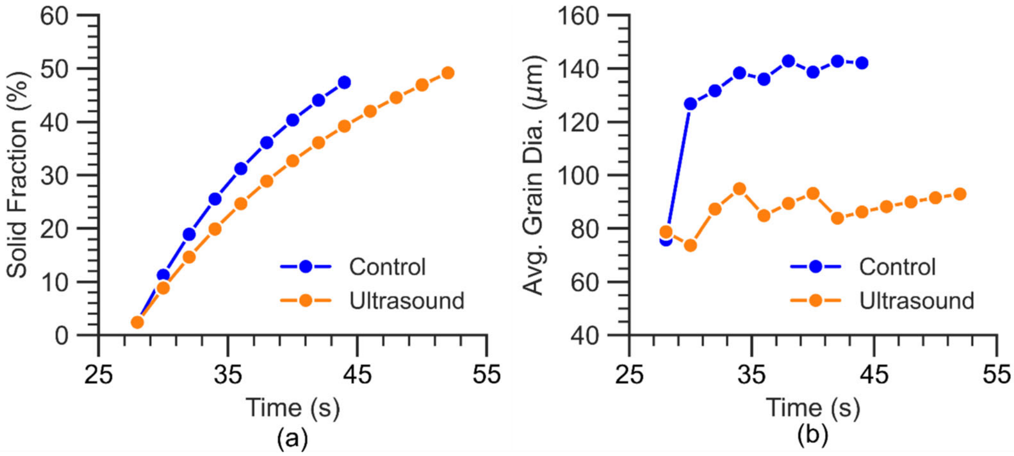

Fig. 12—(*a*) Estimated solid fraction of the α-Al phase, f_S, at a given time calculated using previous work in Ref. 6, (*b*) estimated average diameter of α-Al grains as a function of time, *t*.

helps to validate the use of N_α to estimate the average diameter of α-Al grains *in-situ*.

C. *Mechanisms for Ultrasonically Induced Microstructural Refinement*

The mechanisms by which USMP of molten Al alloys produces globular, refined microstructures can be classified into two categories: those that relate to enhanced nucleation and those that relate to the fragmentation/modification of dendrites. Which mechanisms dominate tend to be defined by the temperature ranges that ultrasound is applied. In general, if ultrasound is applied to fully molten aluminum alloy (*i.e.*, temperatures above the liquidus), then the dominant mechanism is enhanced heterogeneous nucleation.[7–10] On the other hand, if ultrasound is applied to semi-solid aluminum alloy (*i.e.*, temperatures below the liquidus), then the dominant mechanism is the fragmentation of dendrites.[13–15]

In the present work, despite the high energy and brightness of the synchrotron X-ray beam, the two--phase (α-Al + L) system did not produce a strong diffraction intensity of primary α-Al above the diffuse background produced by the liquid phase near the onset of solidification [see Figures 6(c) and (d)]. Thus, in the absence of diffraction data just below the liquidus, it is not possible to comment on the effect ultrasound had on the nucleation rate of primary α-Al grains in early stages of solidification. While the number of primary α-Al grains, N_α, is estimated to increase at a faster rate when ultrasound is applied (see Figure 5), it is not clear whether this increased number of grains is a result of enhanced nucleation or the fragmentation of dendrites. However, we have shown evidence that the application of ultrasound caused the primary α-Al grains to move within the liquid relative to the X-ray beam (see Figure 6). This movement of the primary α-Al grains increases the possibility of grains colliding with one another, causing them to fragment and/or deform, as was previously observed in an *in-situ* radiography study.[14] Furthermore, the movement of the primary α-Al grains appeared to cease at the onset of the Al–Si binary eutectic reaction (or when diffraction data from the eutectic Si phase were first detected). This suggests that there was insufficient remaining liquid phase for the primary α-Al grains to freely move and/or rotate when the total solid fraction reached at least 60 wt pct. Thus, if the fragmentation/deformation of dendrites is the primary mechanism by which the α-Al grains are refined, then the onset of the Al–Si binary eutectic reaction may be the point at which ultrasound is no longer refining the microstructure.

Analysis of the 2D diffraction data also suggests that the application of ultrasound decreased the rate at which the primary α-Al grains grew, particularly over the first few seconds [see Figure 12(b)]. There are a few possible explanations for this slower growth rate.

First, the application of ultrasound homogenizes the melt which affects the solute-gradient-driven dendrite growth. During conventional dendrite growth in a hypoeutectic alloy, such as the one used in this work, there is a greater concentration of solute at the root of the dendrite arms than at the tip of the dendrite. This spatial difference in solute concentration means that the liquidus temperature at the tip of the dendrite is higher (therefore, resulting in greater constitutional undercooling) than that at the root of the dendrite. This gradient results in the dendrite growing faster at the tip than at the root, producing long, dendritic arms. The application of ultrasound, however, causes acoustic streaming within the liquid that can potentially reduce this concentration gradient *via* mixing of the liquid. This active mixing of the melt likely prevented segregation as the specimen solidified and also likely prevented dendrite fragments from floating up due to buoyancy, contrary to what was observed in Reference 14 once ultrasound ceased. Therefore, by homogenizing the chemistry and phase distribution of the melt, ultrasound may suppress dendritic growth and promote slower, more equiaxed grain growth of the primary α-Al grains.

The second reason why ultrasound seems to decrease the growth rate of primary α-Al grains is that the increased number of primary α-Al grains physically obstruct each other's growth. Additionally, if the dendrites are fragmented, then the number of primary α-Al grains would further increase and the average size of the grains would decrease, causing the average growth rate of the grains to be further reduced.

The slower growth rate during the ultrasound experiment, particularly the initial growth rate over the first few seconds, may also be an artifact of the assumptions used to estimate the average grain diameter. According to Eq. [5], the average diameter of the primary α-Al grains, $\overline{d_\alpha}$, is inversely proportional to the cube root of the number of primary α-Al grains, N_α. As shown in Figure 5, the initial rate at which the grains appeared in the ultrasound experiment (2.8 grains per second) is over 5 times greater than the control experiment (0.5 grains per second). Based on Eq. [3], this increased rate of grains appearing would correspond with a slower growth rate when controlling for the solid fraction, f_S. [As a note, f_S is quite similar between the two experiments between $t = 28$ s and $t = 32$ s, see Figure 12(a)]. However, it is possible that the actual number of α-Al grains at a given time was higher than what was estimated from the 2D diffraction patterns, particularly for the control experiment. In the control experiment, the diffraction spots corresponding to primary α-Al grains were quite large, as the grains themselves were quite large. For both *in-situ* experiments, it is possible that multiple α-Al grains may have diffracted at similar azimuthal angles, giving the appearance of a single diffraction spot. It is also possible that there may have been additional α-Al grains that did not satisfy the diffraction condition. This is why N_α should be taken as a lower bound of the estimate of the number of grains present at a given time and not as the absolute number of grains at a given time.

D. *Design of Spatially Fine-Grained Castings*

Local application of ultrasonic melt processing (USMP) to shape castings as they solidify in a mold is capable of producing novel castings with local regions of globular, fine grains. These fine-grained regions can exhibit greater ductility and toughness compared to unmodified regions. As such, local USMP can be used to improve the overall performance of shaped castings by targeting key locations within a casting. For example, it can be used to increase the local toughness of castings at regions of stress concentration due to the geometry of the casting (*e.g.,* sharp corners) or where fatigue loading is a concern. In previous work by the authors,[6] local USMP was demonstrated to refine the microstructure of A356 alloys at distances up to 40 mm away from the ultrasound probe (see Figure 1). The experiments conducted in the present work provide greater understanding of how ultrasonically induced grain refinement is achieved. USMP was shown to slow the initial rate at which primary α-Al grains grew. As additional primary α-Al grains formed and grew, ultrasound continued to refine the microstructure *via* mixing of the solid grains within the surrounding melt. This movement of the primary α-Al grains ceased at the onset of the Al–Si binary eutectic. Therefore, it is recommended that USMP in Al–Si cast alloys be applied from the liquidus temperature to the Al–Si binary eutectic temperature when designing castings with spatially distributed fine-grained regions. For A356 aluminum, this temperature range is from 616 °C to 573 °C. Applying local USMP over this temperature range will allow the greatest possible degree of grain refinement to be achieved.

E. *Future Work*

To the knowledge of the authors, these experiments are some of the first to report the use of *in-situ* SXRD to study USMP in a commercial Al casting alloy and are the first to estimate grain size evolution while ultrasound was applied. The primary challenges in this work were to couple ultrasound to the overall setup and to correlate the microstructural evolution and temperature within the X-ray analyzed volume. As such, there are several opportunities to refine the experimental procedure developed in this study to provide greater clarity on microstructural evolution during solidification in the presence of ultrasound. In particular, the ability to separate the crystalline diffraction peaks from the broad amorphous background in the two-phase liquid + solid regime near the onset of solidification would help elucidate more information about the mechanisms (such as enhanced heterogeneous nucleation) of ultrasound-induced grain refinement. Additionally, it is recommended to collect diffraction data before the specimen has melted and after the specimen has cooled down to room temperature to determine and account for potential slight variations in specimen-detector distance, ambient temperature, and other experimental conditions between and during experiments. This would allow for more accurate calculation of lattice parameter of the phases. Finally, interrupted ultrasonication experiments are proposed to understand how the duration of ultrasonication and the temperature (during solidification) at which it is applied would affect the microstructural evolution. For example, it is not known how long ultrasound must be applied in order to suppress dendritic growth, as previous work in Reference 14 observed dendritic growth in ultrasonically modified α-Al grains once USMP ceased. Furthermore, if USMP were started part-way during solidification so that the primary mechanism for grain refinement is fragmentation of dendrites, it is not known how the grain size would compare to if USMP were applied only above and just below the liquidus, when the primary mechanism for grain refinement is enhanced nucleation. Such interrupted ultrasonication experiments would thus provide further insights to help guide the design of novel castings with spatially distributed fine-grained regions.

V. CONCLUSIONS

In-situ synchrotron X-ray diffraction (SXRD) was used to observe the solidification of a commercial A356 (Al–Si–Mg) aluminum alloy, both with and without ultrasonic melt processing (USMP). To our knowledge, these are the first experiments to combine ultrasound with SXRD for interrogating ultrasonic refinement of the as-cast microstructure in a commercial Al casting alloy. As a complementary set of experiments, laboratory-scale X-ray diffraction experiments were conducted to measure the lattice parameter of the α-Al and Si phases in the same alloy at various temperatures between 25 °C and 523 °C and the resulting calibration data were used to analyze the *in-situ* SXRD data. The following conclusions were obtained:

- Relative to the control experiment (*i.e.*, without ultrasound), USMP produced more powder-like 2D diffraction patterns, with smaller and ~ 2.5 times more diffraction spots corresponding to primary α-Al grains. Analysis of the 2D diffraction patterns estimated that ultrasound reduced the average size of the primary α-Al grains by 36 pct; grain size estimated from this analysis of SXRD data was validated by post-mortem microstructural analysis.
- Relative to the control experiment (*i.e.*, without ultrasound), USMP increased the rate at which primary α-Al grains formed by 5 times and decreased their growth rate by 86 pct. These data, therefore, are some of the first to quantify the evolution of microstructural refinement during the application of ultrasound.
- The greatest reduction in grain size due to USMP was observed during initial solidification at temperatures just below the liquidus. Subsequently, the grains stayed at a relatively constant size. Thus, the application of ultrasound to refine the primary α-Al grains is most effective near the onset of solidification and its continued application during subsequent cooling ensures that the grains maintain their size and do not grow any further.
- USMP enabled the primary α-Al grains to move and rotate during solidification until the Al–Si binary eutectic began to form at which time their (α-Al grains) motion seemed to cease. This absence of motion suggests that any potential microstructural refinement mechanism relying upon the motion or fragmentation of grains is likely not active at temperatures equal to or below the Al–Si binary eutectic temperature.
- The lattice parameters of the α-Al and Si eutectic phases (a_{Al} and a_{Si}, respectively) within the A356 alloy were measured at various temperatures up to 523 °C. Their lattice parameters can be estimated from temperature, T, in Kelvin using the following equations: $a_{\mathrm{Al}} = 6.356 \times 10^{-9}\, T^2 + 1.036 \times 10^{-4}\, T + 4.021$, and $a_{\mathrm{Si}} = 4.891 \times 10^{-9}\, T^2 + 1.133 \times 10^{-5}\, T + 5.430$.

ACKNOWLEDGMENTS

This project was funded by the Department of Energy Vehicle Technologies Office as part of the Lightweight Metals Core Program. This research was conducted at PNNL, under Contract No. DE-AC05-76L01830 with the U.S. Department of Energy, and at Argonne National Laboratory, a U.S. Department of Energy laboratory managed by UChicago Argonne, LLC, under Contract No. DE-AC02-06CH11357. This study used resources of the Advanced Photon Source, a U.S. Department of Energy Office of Science user facility operated for the DOE Office of Science by Argonne National Laboratory under Contract No. DE-AC02-06CH11357. The authors thank Mr. Irving Brown of PNNL for metallographic specimen preparation, Dr. Julian Escobar Atehortua of PNNL for intellectual discussions regarding the analysis, Dr. Peter Kenesei of ANL for assistance with experimental setup and calibration at APS, and Dr. Malte Storm of Helmholtz-Zentrum Hereon for his assistance with Pydidas.

AUTHOR CONTRIBUTIONS

Katherine E. Rader: conceptualization, data curation, formal analysis, investigation, methodology, software, visualization, and writing—original draft. Andrew Chuang: conceptualization, investigation, resources, software, and writing—review & editing. Mark Bowden: investigation, formal analysis, and writing—review & editing. Alan Schemer-Kohrn: investigation, formal analysis, visualization, and writing—review & editing. Jonova Thomas: investigation and writing—review & editing. Dileep Singh: conceptualization, supervision, funding acquisition, and writing—review & editing. Aashish Rohatgi: conceptualization, funding acquisition, investigation, methodology, project administration, supervision, and writing—review & editing.

CONFLICT OF INTEREST

Katherine Rader and Aashish Rohatgi have patent application FORMATION OF METAL ARTICLES USING LOCALIZED SONICATION pending to Assignee: BATTELLE MEMORIAL INSTITUTE. The authors declare that they have no other conflict of interest.

APPENDIX 1: *IN-SITU* SYNCHROTRON X-RAY DIFFRACTION EXPERIMENTAL SETUP & ANALYSIS

A.1.1. Experimental Setup

In-situ diffraction experiments were conducted on beamline 1-ID-E at the Advanced Photon Source at Argonne National Laboratory. An annotated

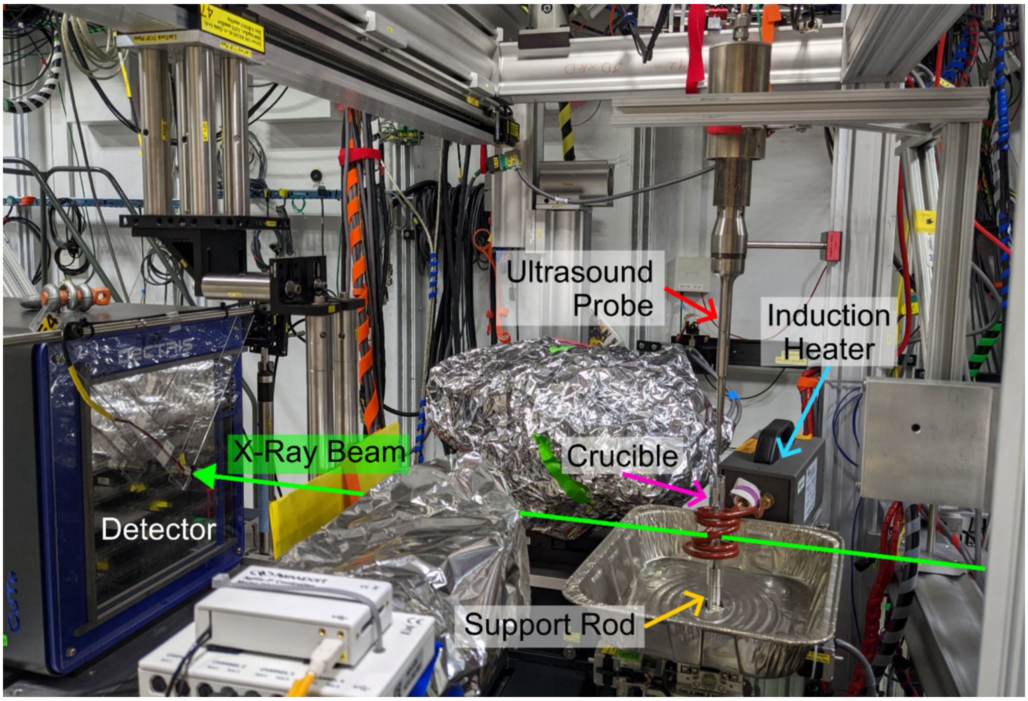

Fig. 13—An annotated photo showing the experimental setup at beamline 1-ID-E at the Advanced Photon Source at Argonne National Laboratory where the *in-situ* X-ray diffraction experiments were conducted.

photograph of the experimental setup is shown in Figure 13. The coordinate system at the beamline was oriented so that the X-ray beam traveled in the + Z direction, the + Y direction pointed up, and the + X direction pointed away from the storage ring. Three independent motorized stages were used to control the positions of the specimen, the heating system, and the ultrasound system. The X and Y positions of the stage supporting the specimens were not changed, but the Z position was raised/lowered to control where the X-ray beam passed through each specimen.

The induction heating system consisted of 5-turn helical-shaped copper tubing induction coils powered by an Ambrell EASYHEAT® 2.4 kW Induction Heating System. The induction coils went around the hourglass-shaped crucible that held each specimen. The crucibles were supported at the bottom *via* a Kovar nickel rod that was threaded onto the motorized stage. At the top and bottom of the crucible, the inner diameter was 14.5 mm. The inner diameter tapered down to 3 mm at the neck of the crucible. The walls of the crucible were 1 mm thick. The X-ray beam passed through the specimen approximately 2 mm above the bottom of the specimen, where it was approximately 4.5 mm thick. The ultrasound system used was a Sonics VCX 750 ultrasonic processor with a tapered, 2-mm-dia. tip probe made of Ti–6Al–4V. The ultrasound probe was inserted into the molten aluminum alloy through the open top of the crucible. A Type-K thermocouple was attached to the tip of the ultrasound probe to measure the temperature of the aluminum alloy. The thermocouple and tip of the ultrasound probe were positioned approximately 10 mm directly above the location, where the X-rays passed through the specimen. A Pilatus3X CdTe 2 M detector positioned normal to the incident X-ray beam was used to collect diffraction data. The beam energy used was 67.416 keV (Ta K-edge) and a 100 × 100 μm square beam was used. A 0.1-second exposure time was used and the gap between frames was 0.01 second. To calibrate the sample-detector geometry and beam center, a CeO_2 foil was used.

For all experiments, 5 V (50 pct of the maximum voltage) was supplied to the induction coils to melt the specimens and heat them above 625 °C. The ultrasound probe was inserted into the specimens for all experiments to maintain constant cooling conditions. For experiments where ultrasonic melt processing was applied, power was supplied to the ultrasonic converter for nearly the entire time that diffraction data were collected and for the entire time that the specimen was solidifying. The ultrasound probe oscillated longitudinally at a frequency of 20 kHz. Power supplied to the ultrasonic converter varied up to 750 W to maintain a constant peak-to-peak amplitude of 82.5 μm at the tip of the ultrasound probe (note that the actual amplitude may have been less).

A.1.1. Analysis

The collected 2D diffraction data were integrated and processed using Pydidas.[29] The algorithm used to integrate the data and fit pseudo-Voigt curves to the α-Al diffraction peaks is shown in Figure 14. First, a

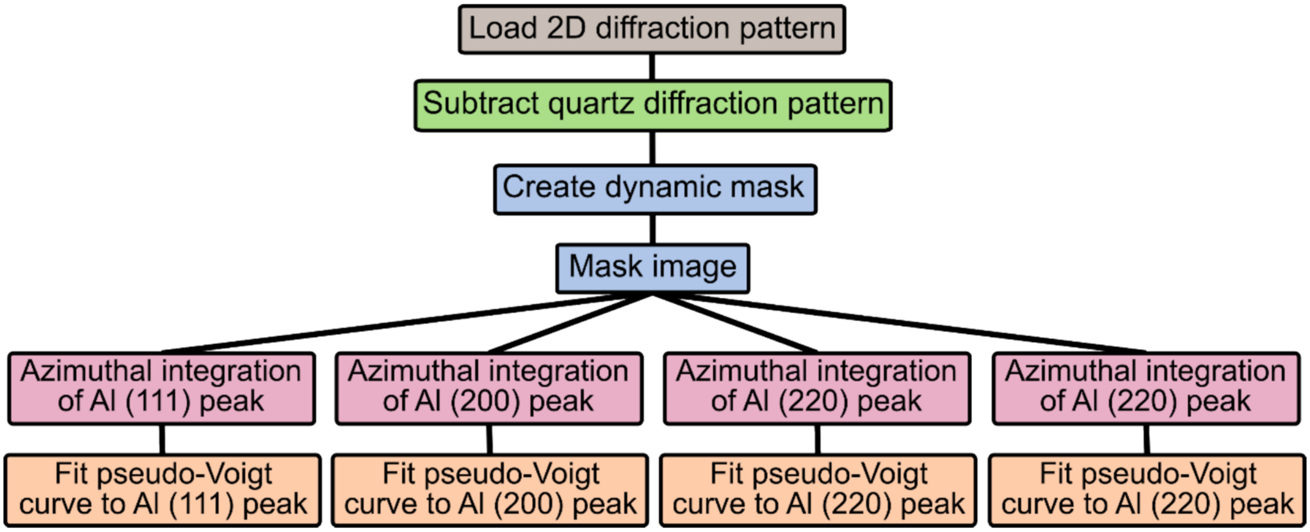

Fig. 14—Algorithm used to process 2D diffraction patterns using Pydidas[29] to quantify α-Al diffraction peaks.

background image of an empty fused-quartz crucible was subtracted from each image. For analysis of the α-Al diffraction peaks, a dynamic mask was applied in addition to the detector mask so that pixels with an intensity of less than 6 counts were not considered. The dynamic mask was necessary for analysis of the α-Al diffraction data on account of the spotty diffraction patterns during the initial stages of solidification. For analysis of the Si diffraction peaks, only the detector mask was necessary. The 2D diffraction data were then integrated about the azimuthal angle, χ, from 0 to 360 deg, with $\chi = 0°$ defined as the positive x axis and positive angular direction is defined as clockwise rotation (see Figure 2). To reduce processing time, only data at radial ranges around the expected locations of the diffraction peaks were integrated with a bin width of 0.01 nm^{-1}. A first-degree polynomial was fit to the background, and a pseudo-Voigt curve was fit to the integrated diffraction data. The location of the peak is defined as the center of the fitted curve, the intensity of the peak is defined as the amplitude of the fitted curve (after subtracting the background), and the breadth of the peak is defined as the full width of the fitted curve at half the maximum amplitude (*i.e.*, FWHM).

While multiple diffraction peaks were detected for both the α-Al and Si phases, the lattice parameters of each phase were calculated using only a single diffraction peak. This is because the non-uniformity of the diffraction rings, particularly during the early stages of solidification, produced integrated 1D diffraction patterns with weak and irregularly shaped diffraction peaks that a pseudo-Voigt curve could not be reliably fit to. Some examples of 1D integrated diffraction data are shown in Figures 6(c) and (d) from the control experiment and the ultrasound experiment, respectively. Before the onset of solidification ($t = 20$ s), there was only a broad diffraction peak corresponding to the amorphous liquid phase. Just after the primary α-Al phase began to form ($t = 30$ s), α-Al diffraction peaks appeared. However, these peaks were relatively weak and did not have strong intensity. The broad diffraction peak corresponding to the amorphous liquid phase was also still present, which could potentially obscure weak α-Al (111) and (200) diffraction peaks. The ultrasound experiment also had the added challenge of intermittent intensity in that the intensity of each diffraction peak rapidly appeared and disappeared [see Figure 6(b)]. For the ultrasound experiment, this meant that some diffraction peaks produced fewer data points compared to the control experiment.

For the α-Al phase, the (200) diffraction peak from the control experiment and the (111) diffraction peak from the ultrasound experiment were used to calculate lattice parameter. The α-Al (200) diffraction peak was chosen for the control experiment because it was one of the earliest diffraction peaks to form and had the strongest intensity. The α-Al (111) diffraction peak was chosen for the ultrasound experiment because a pseudo-Voight curve could be reliably fit to it more often than the other diffraction peaks, especially at times before the onset of the Al–Si binary eutectic. As can be seen in Figure 6(b), the other α-Al diffraction peaks had discernable intensity less frequently during the ultrasound experiment. For both the control and ultrasound experiments, the Si (220) diffraction peak was used to calculate lattice parameter because it had the most reliable pseudo-Voight curve fit analysis.

SUPPLEMENTARY INFORMATION

The online version contains supplementary material available at https://doi.org/10.1007/s11661-025-07939-6.

REFERENCES

1. Ducker Research and Consulting: *2023 North American Light Vehicle Aluminum Content and Outlook*, The Aluminum Association, 2023. https://drivealuminum.org/resources-post/2023-north-american-light-vehicle-aluminum-content-and-outlook/.
2. J.H. Martin, B.D. Yahata, J.M. Hundley, J.A. Mayer, T.A. Schaedler, and T.M. Pollock: *Nat. Lett.*, 2017, vol. 549, pp. 365–69.
3. L.Y. Zhang, Y.H. Jiang, Z. Ma, S.F. Shan, Y.Z. Jia, C.Z. Fan, and W.K. Wang: *J. Mater. Process. Technol.*, 2008, vol. 207, pp. 107–11.
4. L. Yu, X. Liu, Z. Wang, and X. Bian: *J. Mater. Sci.*, 2004, vol. 40, pp. 3865–67.
5. C. Peeratatsuwan and T. Chowwanonthapunya: *Materialwiss. Werkstofftech.*, 2020, vol. 51, pp. 1346–52.
6. K.E. Rader, A.S. Sabau, and A. Rohatgi: *J. Mater. Sci.*, 2023, vol. 58, pp. 17340–61.
7. W. Khalifa, Y. Tsunekawa, and M. Okumiya: *Int. J. Cast Met. Res.*, 2008, vol. 21, pp. 129–34.
8. L. Zhang, D.G. Eskin, and L. Katgerman: *J. Mater. Sci.*, 2011, vol. 26, pp. 5252–59.
9. H.R. Kotadia, M. Qian, D.G. Eskin, and A. Das: *Mater. Des.*, 2017, vol. 132, pp. 266–74.
10. X. Jian, H. Xu, T.T. Meek, and Q. Han: *Mater. Lett.*, 2005, vol. 59, pp. 190–93.
11. G.I. Eskin: *Ultrason. Sonochem.*, 2001, vol. 8, pp. 319–25.
12. D. Eskin: *Mater. Sci. Forum*, 2014, vol. 794–796, pp. 101–06.
13. D. Shu, B. Sun, J.W. Mi, and P.S. Grant: *Metall. Mater. Trans. A*, 2012, vol. 43A, pp. 3755–66.
14. X. Zhang, C. Wang, B. Know, C.M. Schleputz, S. Irvine, and J. Mi: *Acta Mater.*, 2021, vol. 209, p. 116796.
15. H. Huang, D. Shu, Y. Fu, J. Wang, and B. Sun: *Ultrason. Sonochem.*, 2014, vol. 21, pp. 1275–78.
16. I. Tzanakis, W.W. Xu, D.G. Eskin, P.D. Lee, and N. Kotsovinos: *Ultrason. Sonochem.*, 2015, vol. 27, pp. 72–80.
17. W.W. Xu, I. Tzanakis, P. Srirangam, W.U. Mirihanage, D.G. Eskin, A.J. Bodey, and P.D. Lee: *Ultrason. Sonochem.*, 2016, vol. 31, pp. 355–61.
18. F. Wang, D. Eskin, J. Mi, C. Wang, B. Koe, A. King, C. Reinhard, and T. Connolley: *Acta Mater.*, 2017, vol. 141, pp. 142–53.
19. F. Wang, I. Tzanakis, D. Eskin, J. Mi, and T. Connolley: *Ultrason. Sonochem.*, 2017, vol. 39, pp. 66–76.
20. A. Dass, A. Gabourel, D. Pagan, and A. Moridi: *Rev. Sci. Inst.*, 2022, vol. 93, p. 075106.
21. A. Dass, C. Tian, D.C. Pagan, and A. Miridi: *Commun. Mater.*, 2023, vol. 4, p. 76.
22. A. Wakai, A. Das, J. Bustillos, and A. Moridi: *Add. Manuf. Lett.*, 2023, vol. 6, p. 100149.
23. M. Yonemura, T. Osuki, H. Terasaki, Y. Komizo, M. Sato, and A. Kitano: *Mater. Trans.*, 2006, vol. 47, pp. 310–16.
24. B. Schneiderman, A.C. Chuang, P. Kenesi, and Z. Yu: *Sci. Rep.*, 2011, vol. 11, p. 5921.
25. M. Faraji, J.P. Wright, and L. Katgerman: *Mater. Lett.*, 2010, vol. 64, pp. 1016–18.
26. T. Wang, B. Schneiderman, S.J. Clark, A.C. Chuang, Z. Yu, and X. Liu: *Scripta Mater.*, 2024, vol. 242, p. 115946.
27. S. Lampman: in *ASM Handbook, Volume 2A: Aluminum Science and Technology*. K. Anderson, J. Weritz, and J.G. Kaufman, eds., ASM International, 2018, pp. 209–31.
28. M. Warmuzek: in *ASM Handbook, Volume 9: Metallography and Microstructures*. G.F. Vander Voort, ed., ASM International, 2004, pp. 711–51.
29. Y.S. Touloukian, R.K. Kirby, E.R. Taylor, and T.Y.R. Lee: *Thermophysical Properties of Matter- The TRPC Data Series*, vol. 13, IFI/Plenum, New York, 1977.
30. M. Storm: Pydidas- Python diffraction data analysis suite, https://github.com/hereon-GEMS/pydidas, 2023, version 23.7.5, https://doi.org/10.5281/zenodo.7568610.
31. A.P. Hammersley: FIT2D V10.3 Reference Manual, European Synchrotron Radiation Facility, 1998. https://www.esrf.fr/computing/scientific/FIT2D/.
32. S. Kabekkodu, A. Dosen, and T. Blanton: PDF-5+: a comprehensive Powder Diffraction File™ for materials characterization. *Powder Diffr.*, 2024, vol. 39, pp. 47–59. https://doi.org/10.1017/S0885715624000150.